

Microstructure-sensitive uncertainty quantification for crystal plasticity finite element constitutive models using stochastic collocation methods

Anh Tran^{1,*}, Tim Wildey¹, and Hojun Lim²

¹*Scientific Machine Learning, Sandia National Laboratories, Albuquerque, NM 87123, USA*, ²*Computational Materials and Data Science, Sandia National Laboratories, Albuquerque, NM 87123, USA*

Correspondence*:
Anh Tran
anhtran@sandia.gov

ABSTRACT

Uncertainty quantification (UQ) plays a major role in verification and validation for computational engineering models and simulations, and establishes trust in the predictive capability of computational models. In the materials science and engineering context, where the process-structure-property-performance linkage is well known to be the only road mapping from manufacturing to engineering performance, numerous integrated computational materials engineering (ICME) models have been developed across a wide spectrum of length-scales and time-scales to relieve the burden of resource-intensive experiments. Within the structure-property linkage, crystal plasticity finite element method (CPFEM) models have been widely used since they are one of a few ICME toolboxes that allows numerical predictions, providing the bridge from microstructure to materials properties and performances. Several constitutive models have been proposed in the last few decades to capture the mechanics and plasticity behavior of materials. While some UQ studies have been performed, the robustness and uncertainty of these constitutive models have not been rigorously established. In this work, we apply a stochastic collocation (SC) method, which is mathematically rigorous and has been widely used in the field of UQ, to quantify the uncertainty of three most commonly used constitutive models in CPFEM, namely phenomenological models (with and without twinning), and dislocation-density-based constitutive models, for three different types of crystal structures, namely face-centered cubic (fcc) copper (Cu), body-centered cubic (bcc) tungsten (W), and hexagonal close packing (hcp) magnesium (Mg). Our numerical results not only quantify the uncertainty of these constitutive models in stress-strain curve, but also analyze the global sensitivity of the underlying constitutive parameters with respect to the initial yield behavior, which may be helpful for robust constitutive model calibration works in the future.

Keywords: uncertainty quantification, crystal plasticity finite element, constitutive models, stochastic collocation, sparse grid, polynomial chaos expansion

1 INTRODUCTION

Uncertainty quantification (UQ) has been a cornerstone in applied mathematics to verify and validate forward models, with application ranging from subsurface flow, climate change, integrated computational materials engineering (ICME) developments, advanced manufacturing, and many more. In the context of materials design, process-structure-property-performance relationship plays a critical role in establishing the linkage between manufacturing and desired properties, to which materials can be tailored for specific applications. Across the spectrum of length- and time-scales, from quantum to macro-scale, multiple ICME models have been developed in the quest of accurate prediction of materials properties and performance. Notable ICME models for deformation of metals includes, but are not limited to, concurrent or hierarchical couplings of density functional theory, molecular dynamics, kinetic Monte Carlo, dislocation dynamics, crystal plasticity, phase-field, finite element, and any sort of multi-physics and hybrid approaches. Despite its success, there are still much room and open questions for UQ research with respect to microstructure-induced mechanical response in metal alloys.

The concept of ICME models is particularly important because with the predictive capability, engineers can numerically approximate material properties and performance under different operating conditions, without actually performing physical experiments. With the rise of high-performance parallel computing, this step is often hailed as the third paradigm of science Agrawal and Choudhary (2016), supporting prior empirical and experimental, as well as theoretical research. However, as in any forward computational model that relies on deterministic calculations, there is a necessary need to quantify the uncertainty that is associated with the numerical predictions, in order to sufficiently enhance its fidelity and robustness. For the case of crystal plasticity finite element method (CPFEM) as an ICME model that bridges microstructure and materials properties and performance, the question of uncertainty is even more relevant because microstructures are well known to be stochastic, high-dimensional in image or volume representations, and may be anisotropic and heterogeneous.

Numerous UQ studies in computational solid mechanics have been conducted over the last decade. Given the critical importance of optimization and UQ for a wide variety of problems in materials science, several frameworks have been developed, see e.g., Panchal et al. (2013); McDowell (2007); Kalidindi et al. (2016), to provide robust predictions under uncertainty. A comprehensive review of UQ applications in ICME-based simulations can be found in Honarmandi and Arróyave Honarmandi and Arróyave (2020). For example, Zhao et al. Zhao et al. (2022) incorporated measurement and parametric uncertainty to quantify the uncertainty of critical resolved shear stress for hcp Ti alloys from nano-indentation. Lim et al. Lim et al. (2019) investigated the mesh sensitivity and polycrystalline representative volume element (RVE), where initial textures, hardening models, and boundary conditions are uncertain, and showed that an adequate polycrystalline RVE is obtained by capturing 1000 or more grains. Tran and Wildey Tran and Wildey (2020) applied data-consistent inversion method to infer a distribution of microstructure features from a distribution of yield stress, where the push-forward density map via a heteroscedastic Gaussian process approximation is consistent with a target yield stress density. Kotha et al. Kotha et al. (2019a,b, 2020b,a) developed

uncertainty-quantified parametrically homogenized constitutive models to capture uncertainty in microstructure-dependent stress-strain curve, as well as stochastic yield surface, which has been broadly applied for modeling multi-scale fatigue crack nucleation in Ti alloys Ozturk et al. (2019b,a) and for single-crystal Ni-based superalloys with support vector regression as an underlying machine learning model Weber et al. (2020). Sedighiani et al. (2020, 2022) applied genetic algorithm and polynomial approximation to various constitutive models, including phenomenological and dislocation-density-based models. Tran et al. (2019b) applied stochastic collocation (SC) method to quantify uncertainty for dendrite morphology and growth via phase-field model. Acar et al. (2017) proposed a linear programming approach to maximize a mean of materials properties under the assumption of Gaussian distribution for both inputs and outputs. Fernandez et al. (2018) utilized Bayesian inference to quantify the uncertainty in stress-strain curves, where model parameters are treated as random variables. Tallman et al. (2019, 2020) applied Gaussian process regression and the Materials Knowledge System framework to predict a set of homogenized materials properties with uncertainty from a distribution function for crystallography orientations and textures. Inductive design exploration method (IDEM) Ellis and McDowell (2017); McDowell et al. (2009); Choi et al. (2008) has been introduced as a materials design methodology to identify feasible and robust design for microstructure features, which has been broadly applied to many practical problems. From a methodological perspective, numerous applied mathematical UQ techniques have been developed over a few decades. While both intrusive and non-intrusive options are available, non-intrusive polynomial chaos expansion (PCE) Xiu and Karniadakis (2002); Najm (2009), which is also known as non-intrusive spectral projection PCE, is one of the most widely used UQ methods to propagate uncertainty in physical models and computational simulations. Global sensitivity analysis methods, which is arguably constructed on top of the high-dimensional model representation, have also well studied. And apparently, numerous studies connecting PCE and global sensitivity analysis, for example, Sudret (2008), Crestaux et al. (2009), and Saltelli et al. (2010), have been conducted. Despite the fact that numerous UQ application works have been carried out in the materials literature and more specifically, in the structure-property relationship, to the knowledge of the authors, none has been applied to quantify the uncertainty related to the underlying constitutive models used in CPFEM.

In this work, we adopt crystallographic textures from Kocks et al. (1998)(cf. Table I, Chapter 5, pg 185) and Wenk and Van Houtte (2004)(Tables 1 and 2), Raabe et al. (2002), Raabe and Roters (2004), Pham et al. (2017), and Mangal and Holm (2018). We limit the scope of UQ on the microstructure-mechanical property linkage, where the crystal plasticity finite element is widely regarded as the microstructure-aware multi-scale ICME model, and adopt the DREAM.3D Groeber and Jackson (2014) and DAMASK Roters et al. (2019) workflow as previously demonstrated by Diehl et al. (2017), as well as two constitutive models described in Sedighiani et al. (2020, 2022), to perform uncertainty quantification via DAKOTA Eldred (2009); Dalbey et al. (2021).

The rest of the paper is organized as follows. Section 2 introduces PCE and SC as the UQ backbone methodology used in this paper. Section 3 describes the integrated UQ workflow and how they are implemented in practice. Section 4 shows the first case study of 5d UQ for fcc Cu using phenomenological constitutive model with slipping. Section 5 shows the second case study of 16d UQ for hcp Mg using phenomenological constitutive model with slipping and twinning. Section 6

shows the last case study of 7d UQ for bcc W using dislocation-density-based constitutive model. Section 7 discusses and Section 8 concludes the paper, respectively.

2 UNCERTAINTY QUANTIFICATION BACKGROUND

In this section, we describe UQ background for CPFEM. In Section 2.1, we summarize the theoretical foundation for generalized polynomial chaos expansion as a non-intrusive spectral projection method. In Section 2.2, we provide the mathematical background for Smolyak sparse grid construction for high-dimensional interpolation and integration, as well as some comparison to full tensor grid highlighting the computational advantage in SC method. We refer interested readers to Babuška et al. (2007); Nobile et al. (2008); Xiu (2009) for a more rigorous mathematical characterization of the SC method.

2.1 Generalized polynomial chaos expansion

The generalized Wiener-Askey PCE Xiu and Karniadakis (2002) represents the second-order random process $f(\theta)$ as

$$\begin{aligned} f(\theta) &= c_0 I_0 + \sum_{i_1=1}^{\infty} c_{i_1} I_1(\xi_{i_1}(\theta)) \\ &+ \sum_{i_1=1}^{\infty} \sum_{i_2=1}^{\infty} c_{i_1 i_2} I_2(\xi_{i_1}(\theta), \xi_{i_2}(\theta)) \\ &+ \sum_{i_1=1}^{\infty} \sum_{i_2=1}^{\infty} \sum_{i_3=1}^{\infty} c_{i_1 i_2 i_3} I_3(\xi_{i_1}(\theta), \xi_{i_2}(\theta), \xi_{i_3}(\theta)) + \dots, \end{aligned} \quad (1)$$

where $I_n(\xi_{i_1}, \dots, \xi_{i_n})$ denotes the Wiener-Askey polynomial chaos of order n in terms of the random vector $\boldsymbol{\xi} = (\xi_{i_1}, \xi_{i_2}, \dots, \xi_{i_n})$, and c 's are polynomial chaos expansion coefficients to be determined. Without loss of generality, Equation 1 can be rewritten as

$$f(\theta) = \sum_{j=0}^{\infty} \hat{f}_j \Phi_j(\boldsymbol{\xi}(\theta)), \quad (2)$$

where there is a one-to-one correspondence between the function $I_n(\xi_{i_1}, \dots, \xi_{i_n})$ and $\Phi_j(\boldsymbol{\xi})$. $\Phi_j(\boldsymbol{\xi}(\theta))$ are orthogonal polynomials in terms of $\boldsymbol{\xi} := \{\xi_i(\theta)\}_{i=1}^d$, i.e.,

$$\langle \Phi_i \Phi_j \rangle = \langle \Phi_j^2 \rangle \delta_{ij}, \quad (3)$$

where δ_{ij} is the Kronecker delta and $\langle \cdot, \cdot \rangle$ denotes the weighted-average, which is defined as the inner product in the Hilbert space of the variable $\boldsymbol{\xi}$ with respect to the weighting function $\mathbf{W}(\boldsymbol{\xi})$, described in Table 1, as

$$\langle \Phi_i \Phi_j \rangle := \int_{\theta \in \Theta} \Phi_i(\boldsymbol{\xi}) \Phi_j(\boldsymbol{\xi}) \mathbf{W}(\boldsymbol{\xi}) d\boldsymbol{\xi}. \quad (4)$$

Here, \hat{f}_j are the coefficients to be determined. In practice, the number of terms in (2) are truncated after a finite term P , where $P+1 = \frac{(p+n)!}{p!n!}$, where p is the order of PCE, and n is the dimensionality

of the problem, resulting in an approximation for finite PCE, as

$$f(\theta) \approx \sum_{j=0}^P \hat{f}_j \Phi_j(\xi). \tag{5}$$

The PCE coefficients \hat{f}_j is determined by non-intrusive spectral projection of (5) onto the orthogonal polynomial basis $\{\Phi_j\}$ as

$$\hat{f}_j = \frac{\langle f \Phi_j \rangle}{\langle \Phi_j^2 \rangle}. \tag{6}$$

Table 1 describes the relationship between the types of Wiener-Askey polynomial chaos and their corresponding underlying random variables. For uniformly distributed variables ξ used in this paper, the Wiener-Askey scheme Xiu and Karniadakis (2002) requires Legendre polynomials as the polynomial basis $\{\Phi_j\}$.

Table 1. Relationship between the types of Wiener-Askey polynomial chaos and their underlying random variables θ

random variable	probability density function	polynomial	support range
Gaussian	$\frac{1}{\sqrt{2\pi}} e^{-\frac{\theta^2}{2}}$	Hermite	$(-\infty, \infty)$
uniform	$\frac{1}{2}$	Legendre	$[-1, 1]$
beta	$\frac{(1-\theta)^\alpha (1+\theta)^\beta}{2^{\alpha+\beta+1} B(\alpha+1, \beta+1)}$	Jacobi	$[-1, 1]$
gamma	$\frac{\theta^\alpha e^{-\theta}}{\Gamma(\alpha+1)}$	Laguerre	$[0, \infty)$

2.2 Stochastic collocation

Sparse grid methods Novak and Ritter (1996, 1997, 1999); Barthelmann et al. (2000) are a cornerstone in high-dimensional interpolation and integration that have been used in a variety of disciplines. In concert with the generalized polynomial chaos expansion Xiu and Karniadakis (2002) as a non-intrusive spectral projection approach, SC methods Babuška et al. (2007); Nobile et al. (2008); Xiu (2009) are developed to improve the efficiency of the generalized polynomial chaos expansion on high-dimensional problems using Smolyak sparse grids for integration. In the nutshell, the polynomial chaos expansion coefficients are computed based on the sparse grid framework that significantly reduces the effect of the curse-of-dimensionality.

Following Nobile et al. (2008), let $i \geq 1$ and $\{\xi_1^i, \dots, \xi_{m_i}^i\} \subset [-1, 1]$ be a sequence of abscissas, we begin by introducing the one-dimensional Lagrange interpolation operator as

$$\mathcal{U}^i(f)(\xi) = \sum_{j=1}^{m_i} f(\xi_j^i) L_j^i(\xi), \tag{7}$$

where $L_j^i(\xi)$ are the Lagrange polynomials of degree $m_i - 1$, i.e. $L_j^i(\xi) = \prod_{k=1, k \neq j}^{m_i} \frac{(\xi - x_k^i)}{(\xi_j^i - \xi_k^i)}$. The full tensor product formula is perhaps the most straightforward, as

$$\mathcal{U}^{m_1} \otimes \dots \otimes \mathcal{U}^{m_n}(f)(\xi) = \sum_{j_1=1}^{m_1} \dots \sum_{j_n=1}^{m_n} f(\xi_{j_1}^{i_1}, \dots, \xi_{j_n}^{i_n}) \cdot (L_{j_1}^{i_1} \otimes \dots \otimes L_{j_n}^{i_n}), \quad (8)$$

which requires $\prod_{i=1}^n m_i$ functions evaluations. Although simple, a major drawback of full tensor product is that the total number of points grows very fast in high dimensions. Numerous choices of collocation points are possible, such as Gauss-Legendre, Clenshaw-Curtis, Leja, and Gauss-Patterson Nobile et al. (2016). In this work, the weakly-nested Gaussian abscissas (see Section 3.6.2 of Dalbey et al. (2021) and Eldred and Burkardt (2009)), which are zeros of orthogonal polynomials, are utilized for quadrature.

Let $\mathcal{U}^0 = 0$ and for $i \geq 1$, define

$$\Delta^i = \mathcal{U}^i - \mathcal{U}^{i-1}, \quad (9)$$

the isotropic Smolyak quadrature formula Smolyak (1963) is given by

$$\mathcal{A}(q, n) = \sum_{\mathbf{i} \leq q} \Delta^{i_1} \otimes \dots \otimes \Delta^{i_n}, \quad (10)$$

or equivalently as,

$$\mathcal{A}(q, n) = \sum_{q-n+1 \leq |\mathbf{i}| \leq q} (-1)^{q-|\mathbf{i}|} \cdot \binom{n-1}{q-|\mathbf{i}|} \cdot \mathcal{U}^{i_1} \otimes \dots \otimes \mathcal{U}^{i_n}. \quad (11)$$

where $q \geq n$ is an integer denoting the level of the construction Wasilkowski and Woźniakowski (1995). To compute the operator $\mathcal{A}(q, n)$, one needs to evaluate f on the set of points

$$\mathcal{H}(q, n) = \bigcup_{q-n+1 \leq |\mathbf{i}| \leq q} \left(\xi^{i_1} \times \dots \times \xi^{i_n} \right), \quad (12)$$

where $\xi^i = \{\xi_1^i, \dots, \xi_{m_i}^i\} \subset [-1, 1]$ is the collection of abscissas used by the univariate interpolating operator \mathcal{U}^i . This set is a much smaller subset of those required by the full tensor product rule. If the sets are nested, i.e. $\xi^i \subset \xi^{i+1}$, then $\mathcal{H}(q, n) \subset \mathcal{H}(q+1, n)$.

To illustrate the benefits in using the Smolyak sparse grid, compared to the full tensor grid, Table 2 compares the number of simulations required to achieve the same level of accuracy. The dimensionalities are chosen according to the case studies in this paper. The equivalent number points on full tensor grid point is computed as $(2^{\ell+1} - 1)^n$, where ℓ is the corresponding level of sparse grid.

Table 2. The number of collocation points used by sparse grid and full tensor grid.

Level ℓ	$n = 5$		$n = 7$		$n = 16$	
	sparse	full tensor	sparse	full tensor	sparse	full tensor
0	1	1	1	1	1	1
1	11	243	15	2187	33	4.3e+7
2	71	16807	127	823543	577	3.3e+13
3	351	759375	799	170859375	7105	6.5e+18
4	1391	28629151	4047	27512614111	68865	7.2e+23
5	4623	992436543	17263	3938980639167	556801	6.1e+28

2.3 Variance-based global sensitivity analysis

Following Sudret (2008), Crestaux et al. (2009), and Saltelli et al. (2010), we summarize the variance-based global sensitivity analysis based on Sobol’ decomposition as follows. In the spirit of generalized polynomial chaos expansion (i.e. Equation 1 after finite truncation), the Sobol’ decomposition of $f(\boldsymbol{\xi})$ into the summands of increasing dimensions as

$$\begin{aligned}
 f(\xi_1, \dots, \xi_n) &= \hat{f}_0 + \sum_{i=1}^n \sum_{\alpha \in \mathcal{J}_1} \hat{f}_\alpha \Phi(\xi_i) \\
 &+ \sum_{1 \leq i_1 < i_2 \leq n} \sum_{\alpha \in \mathcal{J}_{i_1 i_2}} \hat{f}_\alpha \Phi(\xi_{i_1}, \xi_{i_2}) + \dots \\
 &+ \sum_{1 \leq i_1 < \dots < i_s \leq n} \sum_{\alpha \in \mathcal{J}_{i_1, \dots, i_s}} \hat{f}_\alpha \Phi(\xi_{i_1}, \dots, \xi_{i_s}) \\
 &+ \dots + \sum_{\alpha \in \mathcal{J}_{1, 2, \dots, n}} \hat{f}_\alpha \Phi(\xi_1, \dots, \xi_n).
 \end{aligned}
 \tag{13}$$

Given a model of the form $y = f(\xi_1, \xi_2, \dots, \xi_n)$, with y as a scalar, a variance-based first order effect for a generic factor ξ_i can be written as $\mathbb{V}_{\xi_i} [\mathbb{E}_{\boldsymbol{\xi}_{\sim i}} [y|\xi_i]]$, where $\boldsymbol{\xi}_{\sim i}$ is the vector $\boldsymbol{\xi}$ without the i -th element, i.e. $\boldsymbol{\xi}_{\sim i} = (\xi_1, \dots, \xi_{i-1}, \xi_{i+1}, \dots, \xi_n)$. The main effect sensitivity index (first-order sensitivity coefficient) is written as

$$S_i = \frac{\mathbb{V}_{\xi_i} [\mathbb{E}_{\boldsymbol{\xi}_{\sim i}} [y|\xi_i]]}{\mathbb{V}[y]}.
 \tag{14}$$

It is relatively well-known that

$$\mathbb{E} [\mathbb{V} [y|\boldsymbol{\xi}_{\sim i}]] + \mathbb{V} [\mathbb{E} [y|\boldsymbol{\xi}_{\sim i}]] = \mathbb{V}[y],
 \tag{15}$$

and therefore, the total effect sensitivity index can be obtained as

$$T_i = \frac{\mathbb{E} [\mathbb{V} [y|\boldsymbol{\xi}_{\sim i}]]}{\mathbb{V}[y]} = 1 - \frac{\mathbb{V} [\mathbb{E} [y|\boldsymbol{\xi}_{\sim i}]]}{\mathbb{V}[y]}.
 \tag{16}$$

In global SA, the importance of parameter ξ_i is measured by comparing its variance of the conditional expectation $\mathbb{V}_{\xi_i} [\mathbb{E}_{\boldsymbol{\xi}_{\sim i}} [y|\xi_i]]$ against the total variance $\mathbb{V}[y]$. S_i measures the effect of ξ_i by evaluating the variance contribution of the basis function \hat{f}_i that depends strictly on the set of

variables in ξ_i , while T_i measures the total effect of ξ_i by evaluating the variance contribution of all basis function whose dependencies include ξ_i . For mathematical and implementation details, interested readers are referred to Tang et al. (2010), Weirs et al. (2012), and Crestaux et al. (2009), where most of the computations are based on Monte Carlo sampling ξ . In the context of this manuscript, we can understand ξ as the set of parameters for the underlying constitutive model, whether it is phenomenological or dislocation-density-based, and y as the quantity of interest from the CPFEM model. It should be emphasized that the method used in this study is the mainstream global sensitivity analysis that is widely used in structural reliability studies.

3 UNCERTAINTY QUANTIFICATION WORKFLOW FOR CRYSTAL PLASTICITY

In this paper, we limit the scope of the UQ studies to cases with a unique RVE. As discussed in Section 7, relaxing this restriction will be the subject of future work. DREAM.3D Groeber and Jackson (2014) is used to generate polycrystalline RVE with a specific crystallographic texture, depending on the material considered. DAKOTA Adams et al. (2009) and Python scripts are used to generate inputs for constitutive models, where DAMASK Roters et al. (2019) is employed as the CPFEM forward model. Results are collected and post-processed in DAKOTA.

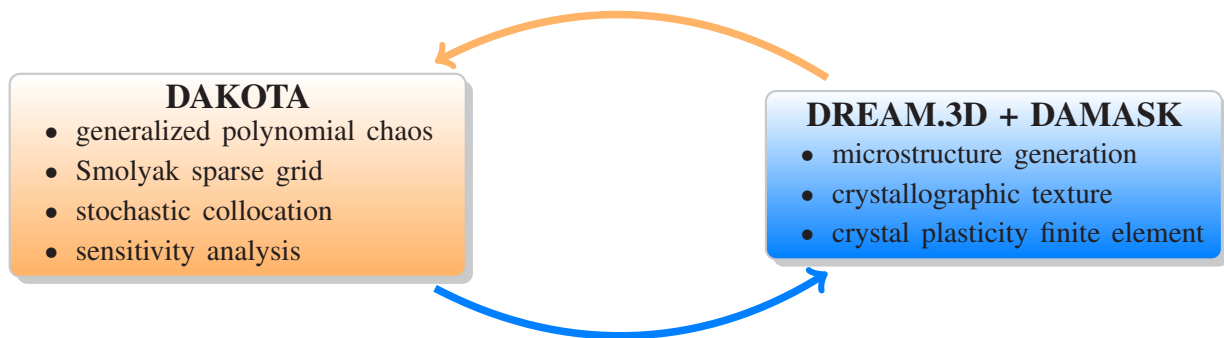


Figure 1. Integrating DAKOTA uncertainty quantification workflow to DREAM.3D and DAMASK crystal plasticity finite element simulations. In this framework, DAKOTA queries input parameters to the DREAM.3D + DAMASK automatic workflow, and receives output(s)/quantity(quantities) of interest from DREAM.3D + DAMASK.

Figure 1 describes the integrated framework coupling DAKOTA uncertainty quantification code and DREAM.3D + DAMASK workflow. Based on the sparse grid construction specifications, such as anisotropic / isotropic, sparse grid level, as well as other sensitivity analysis options, DAKOTA sets up a list of input parameters to be determined and evaluated by the coupled DREAM.3D + DAMASK workflow. The sets of simulations are then deployed on high-performance computing systems and evaluated in parallel to accelerate the process. Typically, for a fixed input parameter vector, an ensemble of microstructural RVEs are used; however, to reduce the computational cost in this study, we limit the scope of our investigation to one microstructure RVE. It should be noted that, if the initial microstructure is fixed, then DAKOTA would interact directly with DAMASK, and the role of DREAM.3D can be conveniently ignored.

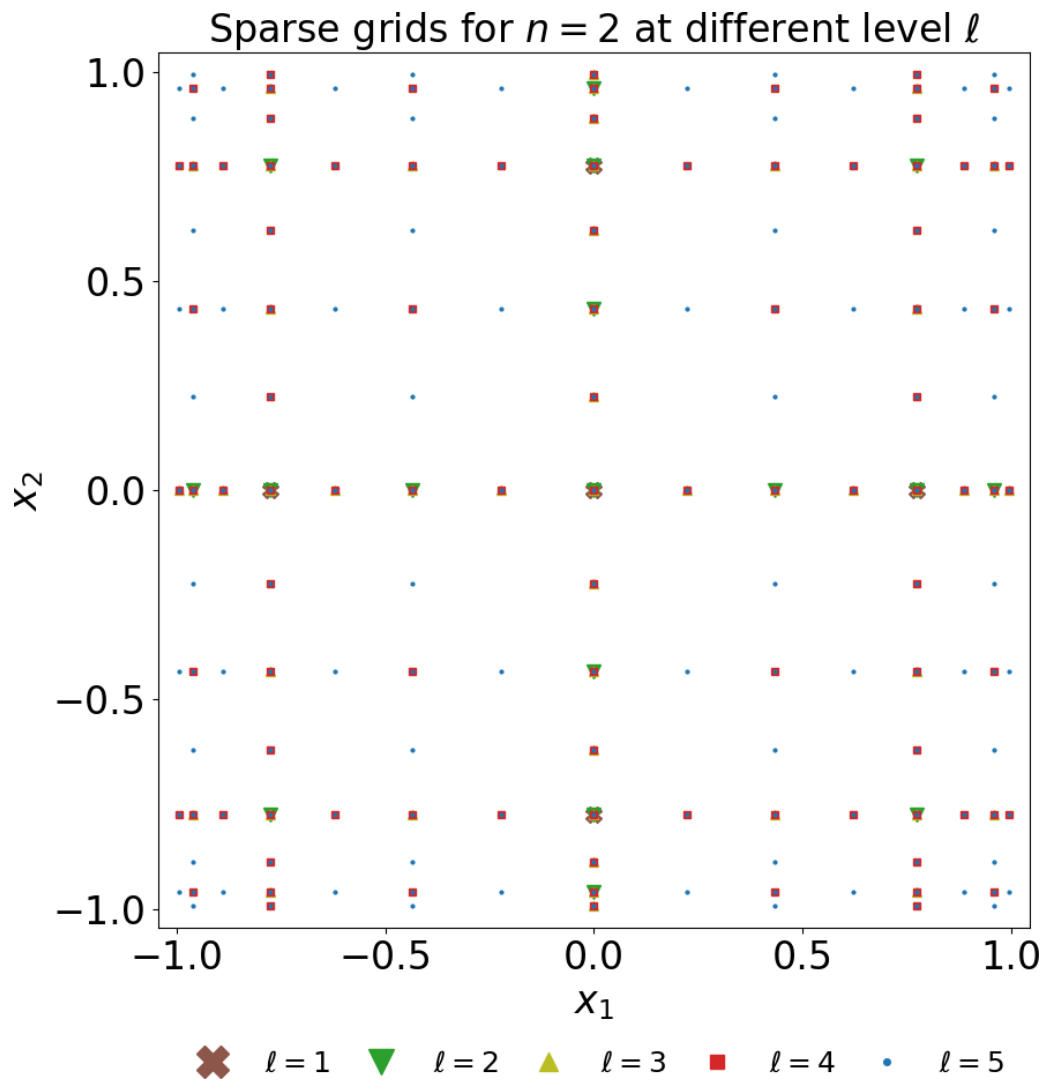


Figure 2. Comparison of 2D Smolyak nested sparse grids at various level ℓ , $1 \leq \ell \leq 5$, with the number of abscissas varies at 5, 17, 49, 97, 161, respectively, using Gaussian abscissas for quadrature.

In this section, Section 3.1 briefly describes the fundamentals of CPFEM model, whereas Section 3.2 describes the UQ workflow for CPFEM based on DAKOTA UQ package as the wrapper and DREAM.3D and DAMASK as a forward ICME model.

3.1 Crystal plasticity model

Consider each point \mathbf{X} in the reference configuration being mapped to the current configuration \mathbf{x} by a linear transformation with the deformation gradient tensor \mathbf{F} , where $\mathbf{F} = \frac{\partial \mathbf{x}}{\partial \mathbf{X}}$. The Lagrangian strain tensor is defined as

$$\mathbf{E} = \frac{1}{2} (\mathbf{F}^T \mathbf{F} - \mathbf{I}). \tag{17}$$

The total deformation gradient \mathbf{F} can be multiplicatively decomposed into an elastic and plastic parts,

$$\mathbf{F} = \mathbf{F}_e \mathbf{F}_p. \tag{18}$$

The velocity gradient, which measures the deformation rate, is defined as

$$\mathbf{L} = \dot{\mathbf{F}}\mathbf{F}^{-1} = \dot{\mathbf{F}}_e\mathbf{F}_e^{-1} + \mathbf{F}_e \left(\dot{\mathbf{F}}_p\mathbf{F}_p^{-1} \right) \mathbf{F}_e^{-1} = \mathbf{L}_e + \mathbf{F}_e\mathbf{L}_p\mathbf{F}_e^{-1}, \quad (19)$$

where \mathbf{L}_p is the plastic velocity gradient evaluated in the intermediate configuration. The second Piola-Kirchoff stress measure \mathbf{S} is defined as

$$\mathbf{S} = \mathbb{C} : \mathbf{E}_e = \frac{\mathbb{C}}{2} \left(\mathbf{F}_e^\top \mathbf{F}_e - \mathbf{I} \right), \quad (20)$$

where \mathbf{E}_e is the elastic Green-Lagrange strain tensor, and \mathbb{C} is the fourth-order stiffness tensor. The plasticity velocity gradient \mathbf{L}_p , driven by the second Piola-Kirchoff \mathbf{S} , controls the evolution of the plastic deformation gradient as

$$\dot{\mathbf{F}}_p = \mathbf{L}_p\mathbf{F}_p. \quad (21)$$

Constitutive equations representing the flow stress, such as the phenomenological slip-based hardening model and the dislocation density-based hardening model, differ on \mathbf{L}_p are calculated based on a specific microstructure and a set of internal state variables. The grain size d in the RVE is a random variable characterized by a log-normal distribution, i.e.,

$$p_D(d; \mu_D, \sigma_D) = \frac{1}{d\sigma_D\sqrt{2\pi}} \exp\left(-\frac{(\ln d - \mu_D)^2}{2\sigma_D^2}\right), \quad (22)$$

where μ_D and σ_D are materials-dependent parameters.

3.2 Forward uncertainty quantification problem

In this work, we consider a forward UQ problem for a fixed set (or ensemble) of microstructures using the SC method, where the set of internal state variables for constitutive model parameters are considered stochastic with some inherent uncertainty. While the non-intrusive PCE approach allows an arbitrary probability density of parameters, in this work, uniform distributions are imposed on the constitutive model parameters due to lack of prior knowledge. With the choice of uniform distributions on bounded intervals, according to the Wiener-Askey scheme shown in Table 1, Legendre polynomials are used to approximate the quantities of interest.

In the initial yield regime, we focus on the the estimated yield strain ε_Y and yield stress σ_Y . From the homogenized stress-strain curve $\varepsilon_{vM} - \sigma_{vM}$ obtained from a CPFEM simulation, the monotonic cubic interpolation via PCHIP method Fritsch and Butland (1984) is utilized to interpolate $\varepsilon_{vM} - \sigma_{vM}$ curve. From the approximated stress-strain curve, an estimation of modulus of elasticity is obtained by simple linear regression. An offset at $\varepsilon = 0.002$ with the estimated modulus of elasticity is drawn, where the coordinates of the intersection are $(\varepsilon_Y, \sigma_Y)$. Statistics of these two quantities of interest are obtained and returned to DAKOTA package.

To set up the UQ study, a pre-processing compilation of constitutive model parameters are obtained from DAKOTA using a numerical toy model. The sets of constitutive model parameters are then appropriately parsed into DAMASK using Python scripts, along with the output of DREAM.3D for setting up the geometric file. With the correct setup of DAMASK simulations, the set of DAMASK simulations are then performed in a massively parallel manner on a high-performance

computing cluster. The post-processing results are then collected from DAMASK, and parsed back to DAKOTA package using a Python interface. DAKOTA then performs the UQ and sensitivity analysis, concluding the UQ workflow for CPFEM based on DREAM.3D and DAMASK.

4 PHENOMENOLOGICAL CONSTITUTIVE MODEL WITH SLIPPING IN FCC CU

4.1 Constitutive law

We adopt the summary and tabulated parameters from Sedighiani et al. (2020, 2022) (Tables 1 and 2). In the phenomenological constitutive model, the shear on each slip system α is modeled as

$$\dot{\gamma}^\alpha = \dot{\gamma}_0 \left| \frac{\tau^\alpha}{\tau_0^\alpha} \right|^n \text{sgn}(\tau^\alpha), \quad (23)$$

where τ_0 is the slip resistance, $\dot{\gamma}_0$ is the reference shear rate, and n determines the strain rate sensitivity of slip. The influence of other slip system α' on the hardening behavior of the slip system α is modeled as

$$\dot{\tau}_0^\alpha = \sum_{\alpha'=1}^{N_s} h_{\alpha\alpha'} |\dot{\gamma}^{\alpha'}|, \quad (24)$$

where $h_{\alpha\alpha'}$ is the hardening matrix, which captures the micromechanical interaction among different slip systems

$$h_{\alpha\alpha'} = q_{\alpha\alpha'} \left[h_0 \left(1 - \frac{\tau_0^\alpha}{\tau_\infty} \right)^a \right], \quad (25)$$

h_0 , a , and τ_∞ are slip hardening parameters for all 12 slip systems in fcc materials. $q_{\alpha\alpha'}$ is a measure for latent hardening with value of 1.0 for coplanar slip system α and α' and 1.4 otherwise.

Table 3. Parameters for Cu used in this case study (cf. Table 4 Roters et al. (2019) and Tables 1 and 2 Sedighiani et al. (2020, 2022)).

variable	description	units	reference value	nature	distribution
C_{11}	elastic constant	GPa	168.3	deterministic	–
C_{12}	elastic constant	GPa	122.1	deterministic	–
C_{44}	elastic constant	GPa	75.7	deterministic	–
$\dot{\gamma}_0$	reference shear rate	s^{-1}	0.003	deterministic	–
τ_0	slip resistance	MPa	1.5	stochastic	$\mathcal{U}[0.5, 3.5]$
τ_∞	saturation stress	MPa	112.5	stochastic	$\mathcal{U}[80, 140]$
h_0	slip hardening parameter	MPa	240	stochastic	$\mathcal{U}[200, 280]$
n	strain rate sensitivity parameter	–	83.3	stochastic	$\mathcal{U}[50, 120]$
a	slip hardening parameter	–	2.0	stochastic	$\mathcal{U}[1, 4]$

4.2 Design of numerical experiments

We conducted our analysis with one RVE shown in Figure 3a, where the crystallographic texture is shown in Figure 3b. Average grain size of $60.9467\mu\text{m}$ is used, where an RVE of size $256\mu\text{m}^3$ is generated. A finite element mesh of 16^3 is created to approximate the microstructure RVE. In DREAM.3D, the texture crystallography of Copper-type with Euler angles $(\phi_1, \theta, \phi_2) = (90^\circ, 35^\circ, 45^\circ)$ is used, the grain size parameters are set as $\mu_D = 4.09$, $\sigma_D = 0.2$, which results

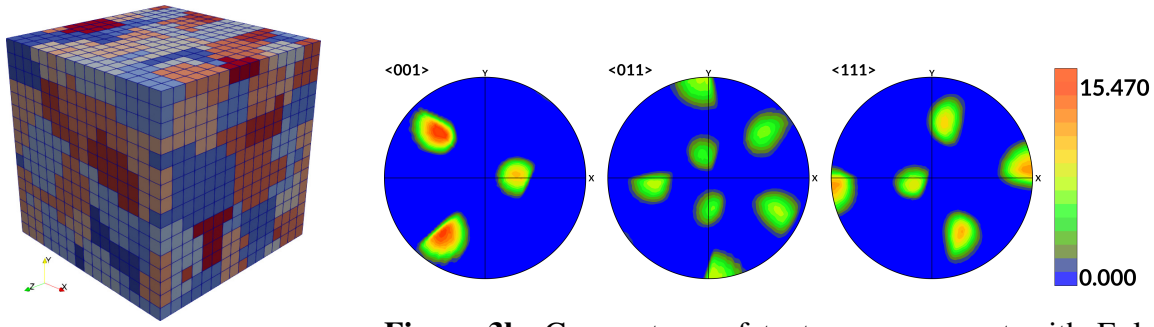


Figure 3a. Representative volume element for Cu.

Figure 3b. Copper-type of texture component with Euler angles $(\phi_1, \theta, \phi_2) = (90^\circ, 35^\circ, 45^\circ)$.

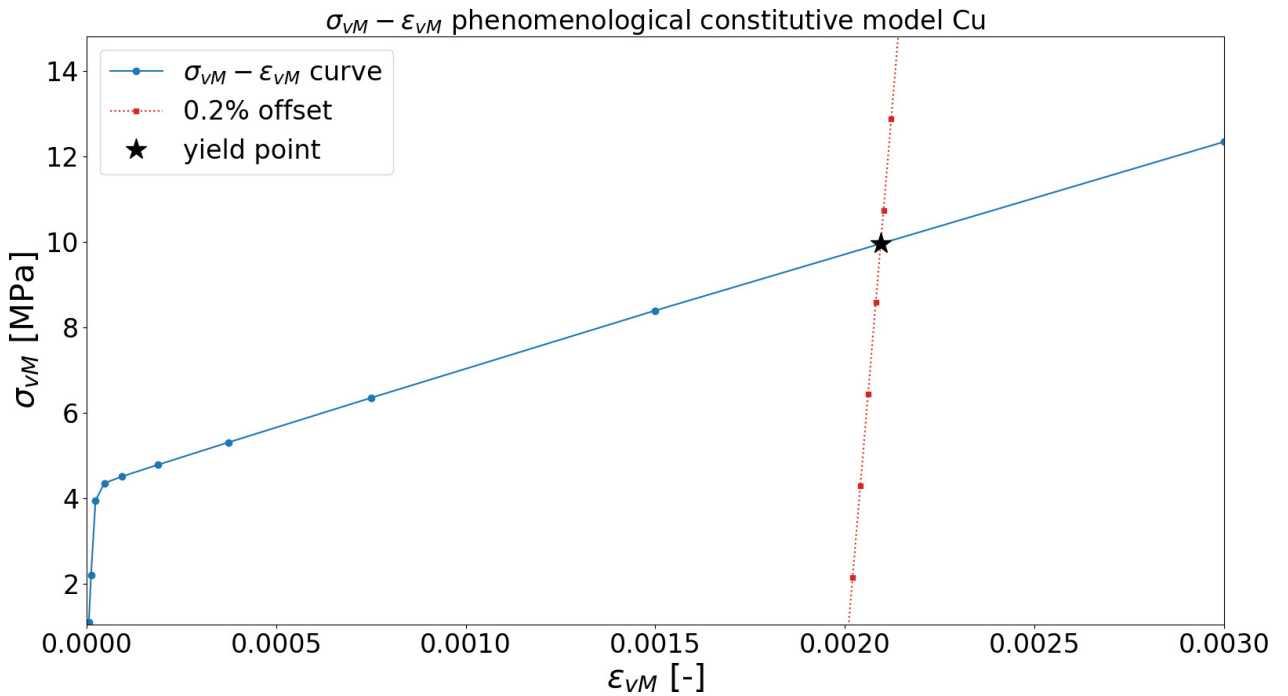


Figure 4. Stress-strain equivalent curve for Cu with default parameters and determination of yield point. Modulus of elasticity is estimated as 188.5919 GPa, while $(\varepsilon_Y, \sigma_Y)$ are estimated as (0.002052, 9.8527 MPa)

in a RVE with 182 grains, shown in Figure 3a. For DAKOTA, we set the sparse grid level $\ell = 3$, dimensionality $n = 5$, which results in 351 inputs. For each set of input parameters, a CPFEM simulation is performed, followed by the post-process. The results are analyzed in the following section. A uniaxial loading condition is applied in the [100] direction with $\dot{\varepsilon} = 10^{-3} \text{s}^{-1}$.

To compare with the default parameter, a single CPFEM simulation is performed with constitutive parameters described in Table 3. The stress-strain equivalent curve is shown in Figure 4. As a reference to experimental data¹, modulus of elasticity for polycrystalline Cu is reported at 110 GPa, whereas its yield strength is reported as 33.3 MPa. Compared to the experiment, the computed

¹ <https://www.matweb.com/search/DataSheet.aspx?MatGUID=9aeb83845c04c1db5126fada6f76f7e>

modulus and yield strength σ_Y are on the same scale, but off roughly by a factor of $1.5\times$, possibly due to different processing conditions resulting in slightly different alloys.

4.3 Numerical results

Figure 5 shows a compilation of stress-strain curve for 351 simulations, where each corresponds to a unique set of constitutive parameters for fcc Cu. As shown in this figure, the constitutive model effects not only the initial yield behavior, but also the modulus of elasticity and the hardening behavior.

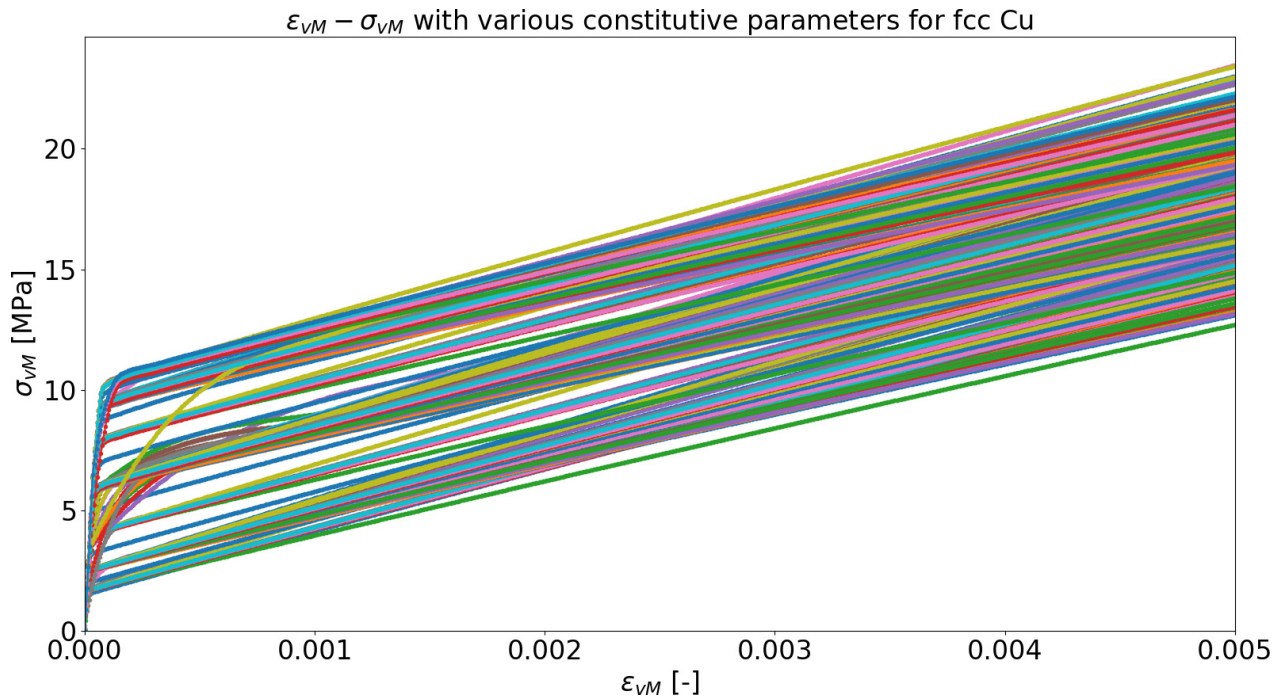


Figure 5. Equivalent $\varepsilon_{vM} - \sigma_{vM}$ plots for fcc Cu.

Figures 6a and 6b show the probability density function for ε_Y and σ_Y , respectively. The mode for ε_Y is approximately 0.00207, whereas the mode for σ_Y is approximately 11.65 MPa. It should be noted that with the current sparse grid level $\ell = 3$, the approximation for ε_Y may be imprecise. One of the possible reasons is that the elastic regime of copper is very small (as shown in Figure 5), and therefore, a more accurate approximation may be required to accurately capture the yield strain.

Figure 7 and Figure 8, respectively, show the Sobol' indices for ε_Y and σ_Y . Ranking from the most influential parameters to the least influential parameters for ε_Y from the Sobol indices for main effects, $T_{\tau_0} = 0.7858$, $T_{h_0} = 0.7035$, $T_n = 0.1922$, $T_a = -0.01038$, and $T_{\tau_\infty} = -0.001983$. Ranking from the most influential parameters to the least influential parameters for σ_Y from the Sobol indices for main effects, $T_{\tau_0} = 0.8258$, $T_{h_0} = 0.4194$, $T_n = 0.07659$, $T_a = -0.01091$, and $T_{\tau_\infty} = -0.0009990$. The order of influential parameters for fcc Cu, regarding the initial yield behavior, is $\tau_0 > h_0 > n > a > \tau_\infty$. Since the main scope of this paper is about the initial yield behavior, it is not surprising that Figure 8 agrees with Figure 7 in terms of Sobol' indices.

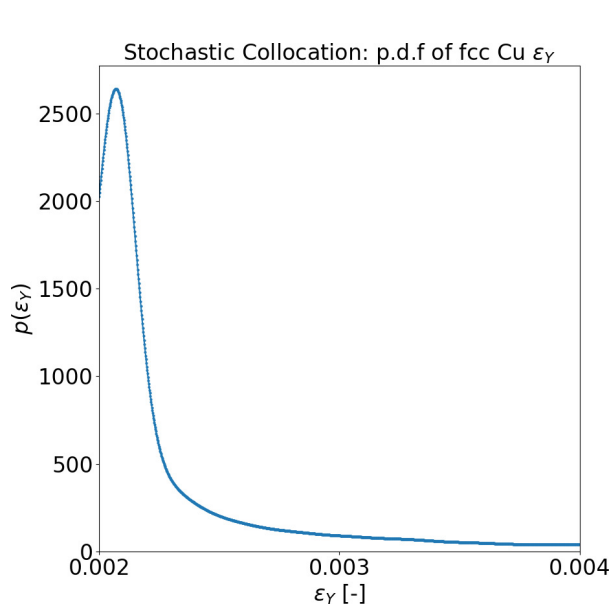


Figure 6a. SC probability density function of ε_Y for fcc Cu.

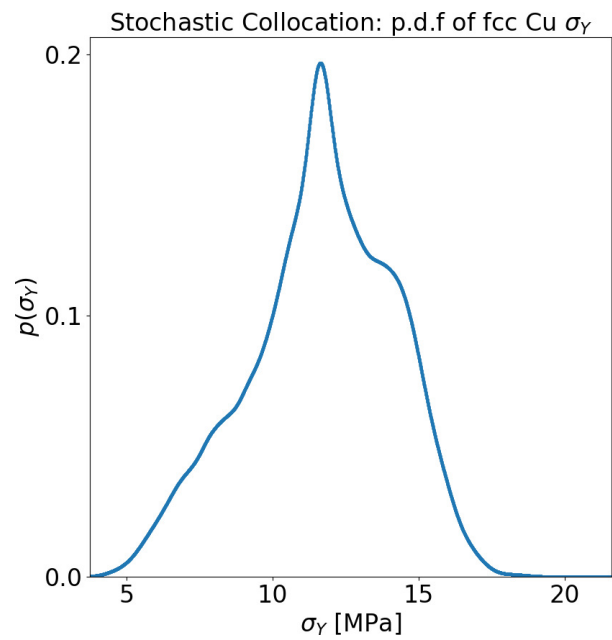


Figure 6b. SC probability density function of σ_Y for fcc Cu.

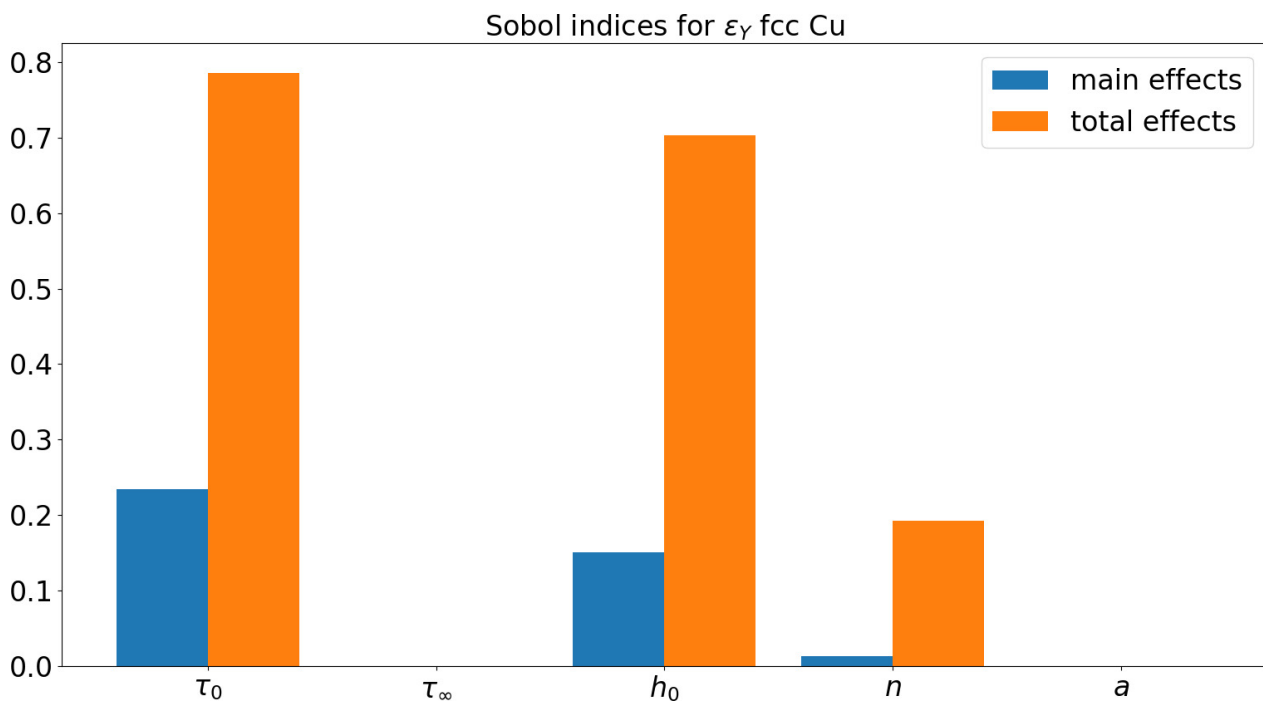


Figure 7. Sobol' indices for ε_Y for fcc Cu.

5 PHENOMENOLOGICAL CONSTITUTIVE MODELS WITH DISLOCATION SLIP AND DEFORMATION TWINNING IN HCP MG

5.1 Constitutive law

Firstly introduced by Hutchinson Hutchinson (1976) and extended for twinning by Kalidindi Kalidindi (1998), the resistance on $\alpha = 1, \dots, N_s$ slip systems evolve from ξ_0 to a

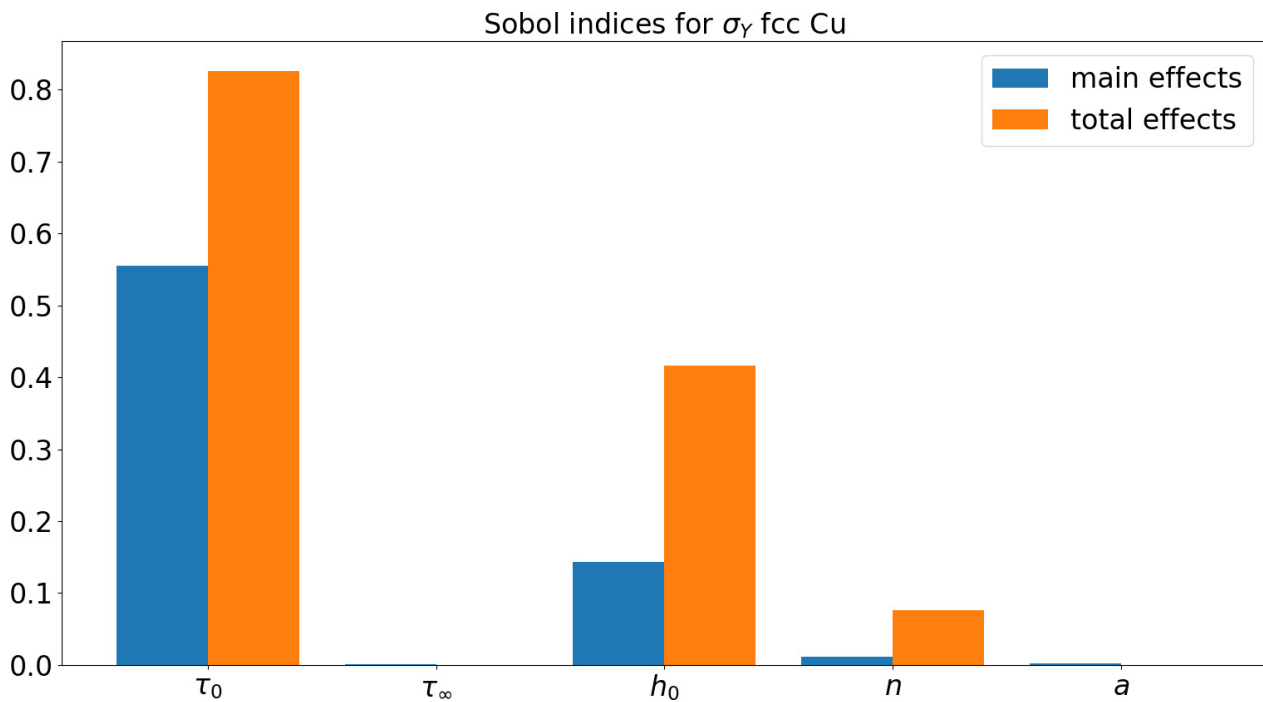


Figure 8. Sobol' indices for σ_Y for fcc Cu.

system-dependent saturation value and depend on shear on slip and twin systems according to

$$\dot{\xi}^\alpha = h_0^{s-s} (1 + c_1 (f_{tw}^{tot})^{c_2}) (1 + h_{int}^\alpha) \left[\sum_{\alpha'=1}^{N_s} |\dot{\gamma}^{\alpha'}| \left| 1 - \frac{\xi^{\alpha'}}{\xi_\infty^{\alpha'}} \right|^a \text{sgn} \left(1 - \frac{\xi^{\alpha'}}{\xi_\infty^{\alpha'}} \right) h^{\alpha\alpha'} \right] + \sum_{\beta'=1}^{N_{tw}} \dot{\gamma}^{\beta'} h^{\alpha\beta'}, \quad (26)$$

where h denotes the components of the slip-slip and slip-twin interaction matrices, h_0^{s-s} , h_{int} , c_1 , c_2 are model-specific fitting parameters and ξ_∞ represents the saturated resistance evolution.

The resistances on the $\beta = 1, \dots, N_{tw}$ twin systems evolve in a similar way,

$$\dot{\xi}^\beta = h_0^{tw-s} \left(\sum_{\alpha=1}^{N_s} |\gamma_\alpha| \right)^{c_3} \left(\sum_{\alpha'=1}^{N_s} |\dot{\gamma}^{\alpha'}| h^{\beta\alpha'} \right) + h_0^{tw-tw} (f_{tw}^{tot})^{c_4} \left(\sum_{\beta'=1}^{N_{tw}} \dot{\gamma}^{\beta'} h^{\beta\beta'} \right), \quad (27)$$

where h_0^{tw-s} , h_0^{tw-tw} , c_3 , and c_4 are model-specific fitting parameters. Shear on each slip system evolves at a rate of

$$\dot{\gamma}^\alpha = (1 - f_{tw}^{tot}) \dot{\gamma}_0^\alpha \left| \frac{\tau^\alpha}{\xi^\alpha} \right|^n \text{sgn}(\tau^\alpha). \quad (28)$$

where slip due to mechanical twinning accounting for the unidirectional character of twin formation is computed slightly differently,

$$\dot{\gamma} = (1 - f_{tw}^{tot}) \dot{\gamma}_0 \left| \frac{\tau}{\xi} \right|^n \mathcal{H}(\tau), \quad (29)$$

where \mathcal{H} is the Heaviside step function. The total twin volume is calculated as

$$f_{\text{tw}}^{\text{tot}} = \max \left(1.0, \sum_{\beta=1}^{N_{\text{tw}}} \frac{\gamma^{\beta}}{\gamma_{\text{char}}^{\beta}} \right), \quad (30)$$

where γ_{char} is the characteristic shear due to mechanical twinning and depends on the twin system. Interested readers are referred to Section 6.2.2 from Roters et al. (2019).

Table 4. Parameters for Mg used in this case study (cf. Tables 7 and 8 Sedighiani et al. (2020, 2022), Wang et al. (2014); Tromans (2011); Agnew et al. (2006)).

variable	description	units	reference value	nature	distribution
c/a	lattice parameter ratio	–	1.635	deterministic	–
C_{11}	elastic constant	GPa	59.3	deterministic	–
C_{12}	elastic constant	GPa	61.5	deterministic	–
C_{44}	elastic constant	GPa	16.4	deterministic	–
C_{44}	elastic constant	GPa	25.7	deterministic	–
C_{44}	elastic constant	GPa	21.4	deterministic	–
$\dot{\gamma}_0$	twinning reference shear rate	s^{-1}	0.001	deterministic	–
$\dot{\gamma}_0$	slip reference shear rate	s^{-1}	0.001	deterministic	–
$\tau_{0,\text{basal}}$	basal slip resistance	MPa	10	stochastic	$\mathcal{U}[5, 30]$
$\tau_{0,\text{pris}}$	prismatic slip resistance	MPa	55	stochastic	$\mathcal{U}[30, 60]$
$\tau_{0,\text{pyr}\langle a \rangle}$	pyramidal $\langle a \rangle$ slip resistance	MPa	60	stochastic	$\mathcal{U}[50, 90]$
$\tau_{0,\text{pyr}\langle c+a \rangle}$	pyramidal $\langle c + a \rangle$ slip resistance	MPa	60	stochastic	$\mathcal{U}[50, 110]$
$\tau_{0,\text{T1}}$	tensile twin resistance	MPa	45	stochastic	$\mathcal{U}[35, 70]$
$\tau_{0,\text{C2}}$	compressive twin resistance	MPa	80	stochastic	$\mathcal{U}[60, 120]$
$\tau_{\infty,\text{basal}}$	basal saturation stress	MPa	45	stochastic	$\mathcal{U}[30, 60]$
$\tau_{\infty,\text{pris}}$	prismatic saturation stress	MPa	135	stochastic	$\mathcal{U}[100, 160]$
$\tau_{\infty,\text{pyr}\langle a \rangle}$	pyramidal $\langle a \rangle$ saturation stress	MPa	150	stochastic	$\mathcal{U}[120, 180]$
$\tau_{\infty,\text{pyr}\langle c+a \rangle}$	pyramidal $\langle c + a \rangle$ saturation stress	MPa	150	stochastic	$\mathcal{U}[120, 180]$
$h_0^{\text{tw}-\text{tw}}$	twin-twin hardening parameter	MPa	50	stochastic	$\mathcal{U}[30, 80]$
$h_0^{\text{s}-\text{s}}$	slip-slip hardening parameter	MPa	500	stochastic	$\mathcal{U}[100, 200]$
$h_0^{\text{tw}-\text{s}}$	twin-slip hardening parameter	MPa	150	stochastic	$\mathcal{U}[400, 680]$
n_s	slip strain rate sensitivity parameter	–	10	stochastic	$\mathcal{U}[15, 35]$
n_{tw}	twinning strain rate sensitivity parameter	–	5	stochastic	$\mathcal{U}[3, 8]$
a	slip hardening parameter	–	2.5	stochastic	$\mathcal{U}[2, 4]$

5.2 Design of numerical experiments

Similar to the previous section we restrict the scope to one RVE shown in Figure 9a, where the crystallographic texture is shown in Figure 9b. Average grain size of $204.037\mu\text{m}$ is used, where an RVE of size $2048\mu\text{m}^3$ is generated. A mesh of 64^3 is created to approximate the microstructure RVE. In DREAM.3D, the texture crystallography with Euler angles $(\phi_1, \theta, \phi_2) = (90^\circ, 0^\circ, 0^\circ)$ is used, the grain size parameters are set as $\mu_D = 5.2983$, $\sigma_D = 0.2$, which results in a RVE with 1706 grains, shown in Figure 9a. For DAKOTA, we set the sparse grid level $\ell = 2$, dimensionality $n = 16$, which results in 577 inputs. For each set of input parameters, a CPFEM simulation is performed, followed by the post-processing steps. The results are analyzed in the following section. A uniaxial loading condition is applied in the $[100]$ direction with $\dot{\epsilon} = 10^{-3}\text{s}^{-1}$.

To compare with the default parameter, a single CPFEM simulation is performed with constitutive parameters described in Table 4. The stress-strain equivalent curve is shown in Figure 10. As a

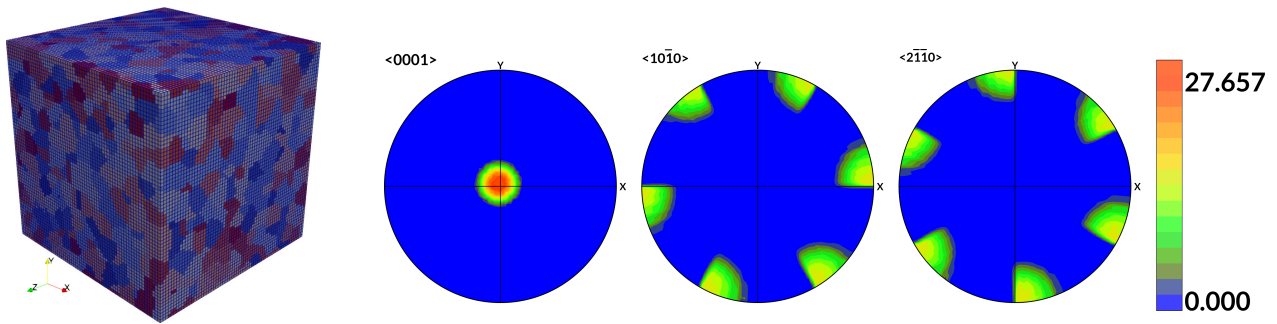


Figure 9a. Representative volume element for Mg.

Figure 9b. Magnesium texture component with Euler angles $(\phi_1, \theta, \phi_2) = (90^\circ, 0^\circ, 0^\circ)$ Mangal and Holm (2018).

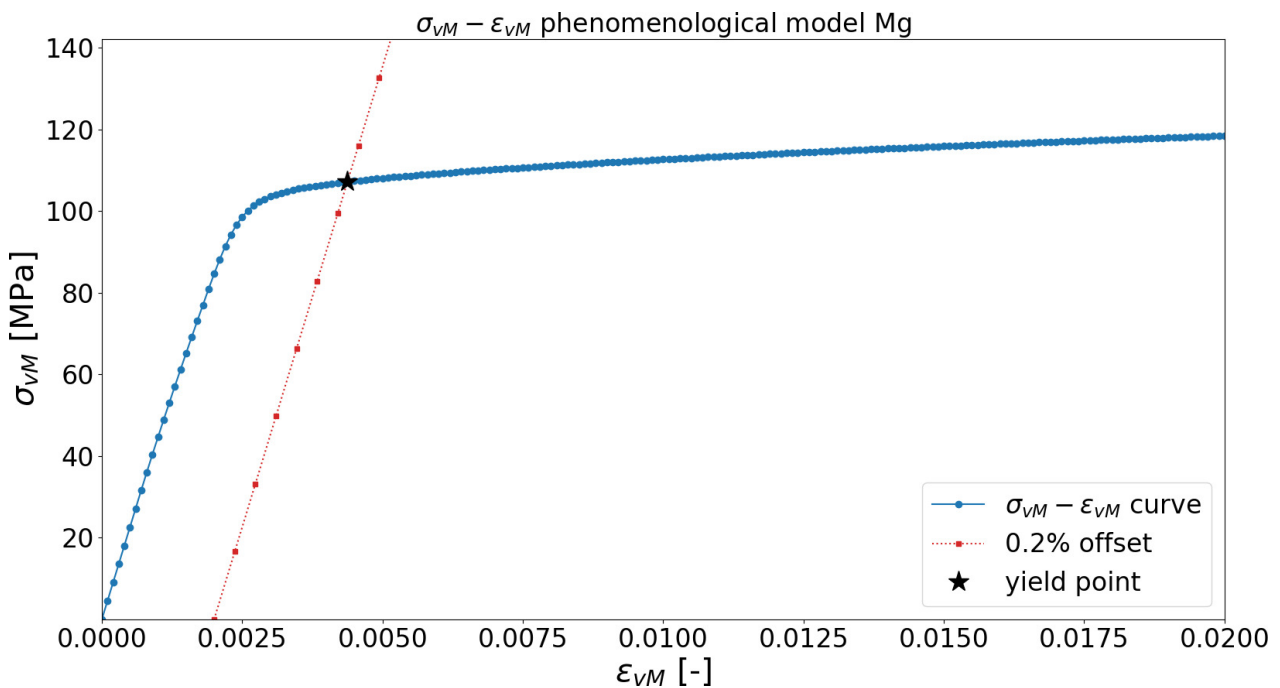


Figure 10. Stress-strain equivalent curve for Mg with default parameters and determination of yield point. Modulus of elasticity is estimated as 45.1172 GPa, while (ϵ_Y, σ_Y) are estimated as (0.004375, 107.2 MPa)

reference to experimental data², the modulus of elasticity for polycrystalline Mg is reported at 44 GPa, whereas its yield strength is reported as 90-105 MPa. Compared to the experiment, the computed modulus and yield strength σ_Y are well calibrated, as the computational results agree very well with the experimental data.

5.3 Numerical results

Figure 11 shows a compilation of stress-strain curves for 577 simulations, where each corresponds to a unique set of constitutive parameters for hcp Mg. As shown in this figure, the constitutive model

² <https://www.matweb.com/search/DataSheet.aspx?MatGUID=7b49605d472d40d393ffe87ea224980c>

has a minor effect on the effective modulus of elasticity, and more profound effect on the yield stress σ_Y .

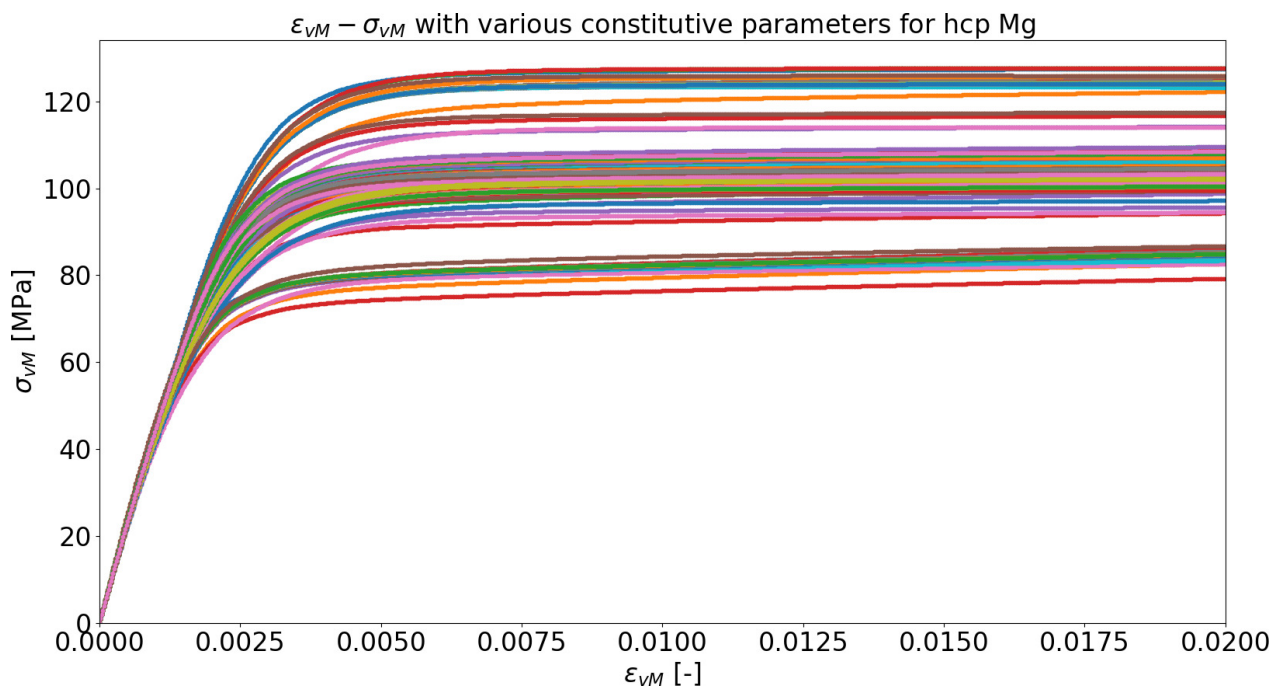


Figure 11. Equivalent $\varepsilon_{vM} - \sigma_{vM}$ plots for hcp Mg.

Figure 12a and Figure 12b, respectively, show the probability density function for ε_Y and σ_Y . The mode for ε_Y is approximately 0.0054, whereas the mode for σ_Y is approximately 99 MPa. The uncertainty explained in σ_Y reasonably agree with experimental data.

Figure 13 and Figure 14, respectively, show the Sobol' indices for ε_Y and σ_Y . Ranking from the most influential parameters to the least influential parameters for ε_Y from the Sobol indices for main effects, $T_{\tau_0, \text{basal}} = 0.5668$, $T_{\tau_0, \text{C2}} = 0.4772$, $T_{n_{\text{tw}}} = 0.2439$, $T_{h_0^{s-s}} = 0.1021$, $T_{\tau_{\infty}, \text{basal}} = 0.07249$, $T_{\tau_0, \text{pyr}\langle a \rangle} = 0.6131$, $T_{n_s} = 0.02082$, $T_{\tau_{\infty}, \text{pyr}\langle a \rangle} = 0.01091$. Ranking from the most influential parameters to the least influential parameters for σ_Y from the Sobol indices for main effects, $T_{\tau_0, \text{C2}} = 0.3729$, $T_{n_{\text{tw}}} = 0.3684$, $T_{\tau_0, \text{basal}} = 0.3566$, $T_{\tau_0, \text{pyr}\langle a \rangle} = 0.1181$, $T_{\tau_{\infty}, \text{basal}} = 0.1064$, $T_{h_0^{s-s}} = 0.1061$, $T_{\tau_0, \text{pris}} = 0.03861$. Compared to Sedighiani et al. Sedighiani et al. (2020, 2022), our analysis shows some agreements, but mostly differ in the set of sensitive parameters. Possible explanations are due to (1) different quantities of interest and (2) methodological approach: Sedighiani et al. Sedighiani et al. (2020, 2022) studies are conducted based on ANOVA, whereas our approach relies on global sensitivity analysis with Sobol' indices.

6 DISLOCATION-DENSITY-BASED CONSTITUTIVE MODEL FOR BCC W

6.1 Constitutive law

For the sake of completeness, we adopt the dislocation-density-based constitutive law description from Cerededa et al. Cerededa et al. (2016, 2015), Stukowski et al. Stukowski et al. (2015), and summarize it here. Interested readers are further referred to Cerededa et al. Cerededa et al. (2016,

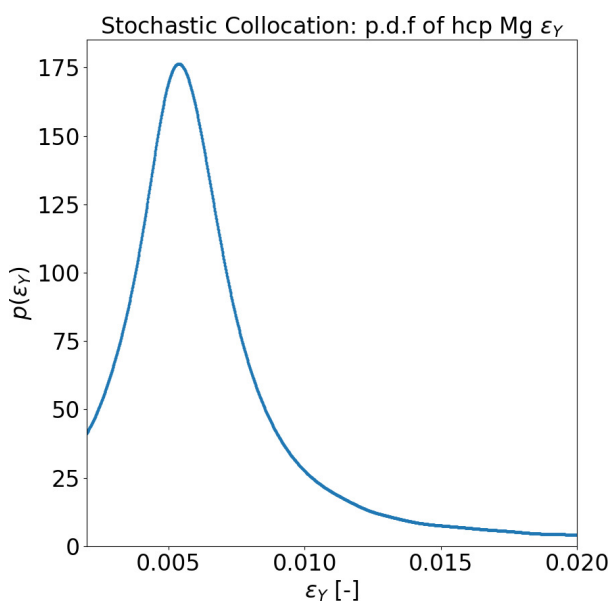


Figure 12a. SC probability density function of ϵ_Y for hcp Mg.

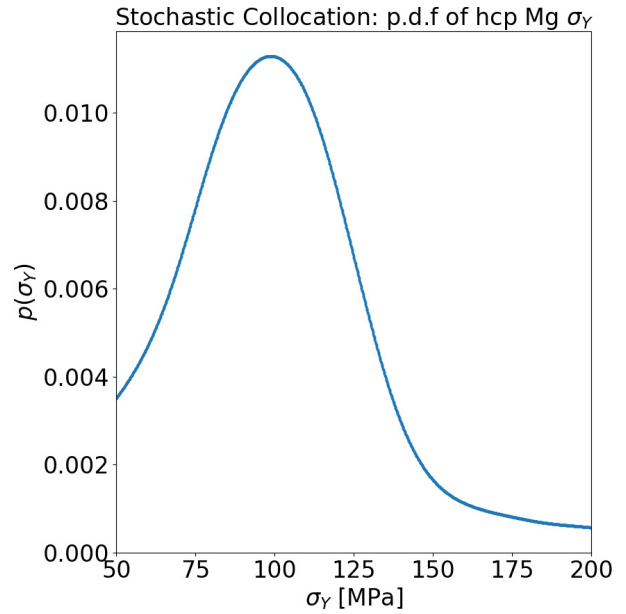


Figure 12b. SC probability density function of σ_Y for hcp Mg.

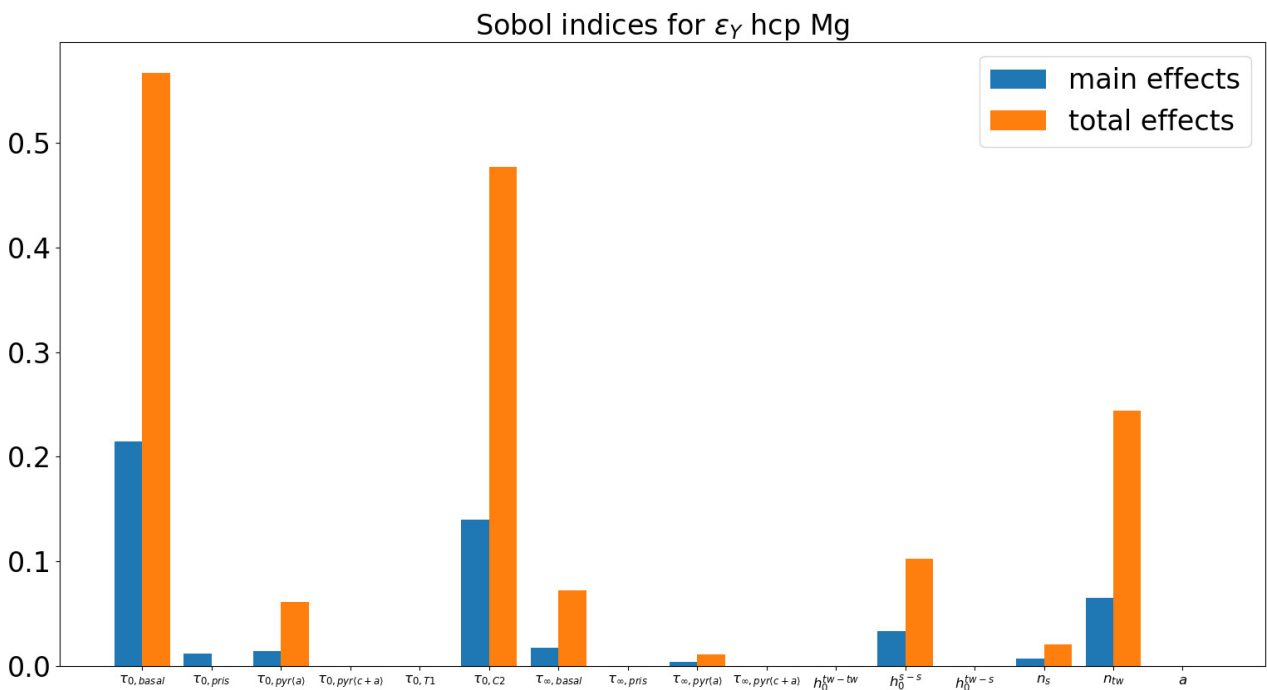


Figure 13. Sobol' indices for ϵ_Y for hcp Mg.

2015, 2013), Stukowski et al. (2015), especially Cereceda et al. (2016) for a complete formulation.

It is assumed that all the plastic deformation is due to dislocation slip, i.e.

$$L_p = \sum_a \dot{\gamma}^\alpha P_S^\alpha \tag{31}$$

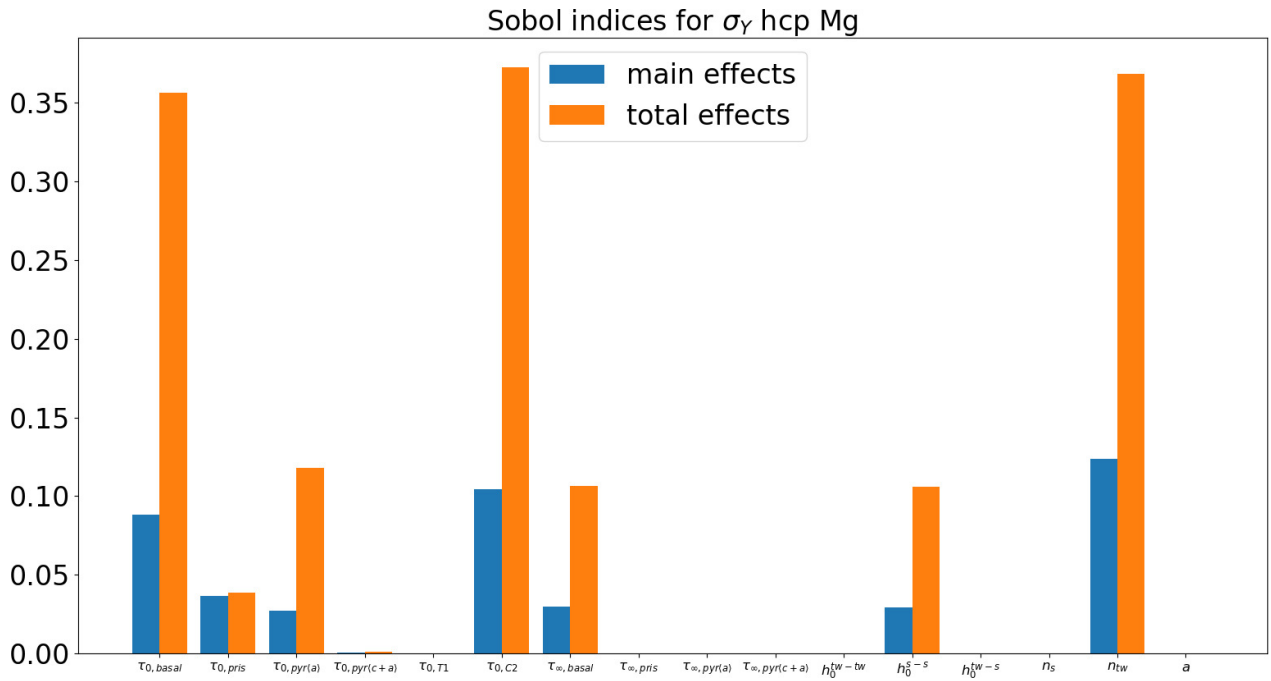


Figure 14. Sobol' indices for σ_Y for hcp Mg.

where α is a slip system, \mathbf{m}^α and \mathbf{n}^α are unit vectors in the normalized slip direction and the normal to the slip plane of the system α , respectively, $\mathbf{P}_S^\alpha = \mathbf{m}^\alpha \otimes \mathbf{n}^\alpha$ is a Schmid geometric projection tensor. The resolved shear stress of slip system α include both Schmid and non-Schmid factors as

$$\tau^\alpha = \mathbf{P}_{total}^\alpha : \sigma = (\mathbf{P}_S^\alpha + \mathbf{P}_{T/AT}^\alpha + \mathbf{P}_{ng}^\alpha) : \sigma \quad (32)$$

, where $\mathbf{P}_{T/AT}^\alpha = a_1 \mathbf{m}^\alpha \otimes \mathbf{n}_1^\alpha$ is a non-Schmid tensor representing twinning and anti-twinning asymmetry and the effects due to non-glide stress components, $\mathbf{P}_{ng}^\alpha = a_2 (\mathbf{n}^\alpha \otimes \mathbf{m}^\alpha) \otimes \kappa^\alpha + a_3 (\mathbf{n}_1^\alpha \otimes \mathbf{m}^\alpha) \otimes \mathbf{n}_1^\alpha$. \mathbf{n}_1^α forms an angle of -60° with the reference slip plane defined by \mathbf{n}^α and changes sign with the direction of slip on each glide plane Koester et al. (2012). a_1, a_2, a_3 are calibrated material-dependent constants. The shear rate $\dot{\gamma}^\alpha$ is given by the Orowan equation

$$\dot{\gamma}^\alpha = b \rho^\alpha v_s(\tau^\alpha, T), \quad (33)$$

where $b = a_0 \sqrt{3}/2$ is the magnitude of the Burgers vector, a_0 is the lattice parameter, T is the absolute temperature, ρ^α is the density of mobile screw dislocations in slip system α , and $v_s(\tau^\alpha, T)$ is the screw dislocation velocity, which captures the thermally activated character of dislocation motion.

Under the assumption that kink relaxation is significantly faster than kink-pair nucleation, the total time t_t required for a kink pair to form and sweep a rectilinear screw dislocation segment of length λ^α is

$$t_t = t_n + t_k = J(\tau^\alpha, T)^{-1} + \frac{\lambda^\alpha - w}{2v_k(\tau^\alpha, T)}, \quad (34)$$

where t_n is the mean time to nucleate a kink pair, t_k is the time needed for a kink to sweep half a segment length, J is the kink-pair nucleation rate, w is the kink-pair separation, v_k is the kink velocity.

The kink-pair nucleation rate is modeled by an Arrhenius formulation as

$$J(\tau^\alpha, T) = \frac{v_0(\lambda^\alpha - w)}{b} \exp\left(-\frac{\Delta H_{\text{kp}}(\tau^\alpha)}{kT}\right), \quad (35)$$

where v_0 is an attempt frequency, ΔH_{kp} is the activation enthalpy of a kink pair stress τ^α , k is Boltzmann's constant. The kink velocity is modeled as

$$v_k(\tau^\alpha, T) = \frac{b\tau^\alpha}{B(T)}, \quad (36)$$

where B is simplified to a constant. The dislocation velocity can be modeled as

$$v_s = \frac{h}{t_t} = \frac{h}{t_n + t_k} = \frac{2bh\tau^\alpha v_0(\lambda^\alpha - w) \exp\left(-\frac{\Delta H_{\text{kp}}}{kT}\right)}{2b^2\tau^\alpha + v_0B(\lambda^\alpha - w)^2 \exp\left(-\frac{\Delta H_{\text{kp}}}{kT}\right)}, \quad (37)$$

where $h = a_0\sqrt{6}/3$ is the distance between two consecutive Peierls valleys. When $t_k \ll t_n$, $v_0B(\lambda^\alpha - w)^2 \exp\left(-\frac{\Delta H_{\text{kp}}}{kT}\right) \rightarrow 0$, and the common diffusive velocity expression is recovered

$$v_s = v_0h \frac{(\lambda^\alpha - w)}{b} \exp\left(-\frac{\Delta H_{\text{kp}}(\tau^\alpha)}{kT}\right) \text{sgn}(\tau^\alpha). \quad (38)$$

It is further elaborated in Sedighiani et al. (2020) that

$$\Delta H_{\text{kp}}(\tau^\alpha) = \Delta H_{\text{kp}} \left[1 - \left(\frac{\tau^\alpha}{\tau_0^*} \right)^p \right]^q, \quad (39)$$

where p and q determine the shape of the short-range activation energy.

Following the Kocks-Mecking family of dislocation density evolution models Mecking and Kocks (1981), the mobile dislocation density on slip system α evolves in time is modeled as

$$\dot{\rho}^\alpha = \dot{\rho}_{\text{mult}}^\alpha + \dot{\rho}_{\text{ann}}^\alpha, \quad (40)$$

with the initial dislocation density $\rho^\alpha(t=0) = \rho_0^\alpha$. Dislocation multiplication is proportional to the inverse mean free path of the dislocation λ^α and the plastic strain rate, as

$$\dot{\rho}_{\text{mult}}^\alpha = \frac{\dot{\gamma}^\alpha}{b\lambda^\alpha}. \quad (41)$$

λ^α is defined as

$$\frac{1}{\lambda^\alpha} = \frac{1}{d_g} + \frac{\sqrt{\rho_f^\alpha}}{c}, \quad (42)$$

where d_g is the grain size, c is a hardening constant, ρ_f^α is the forest dislocation density and calculated as

$$\rho_f^\alpha = \sum_{\beta} \rho^\beta |\mathbf{n}^\alpha \cdot \mathbf{m}^\beta| \quad (43)$$

Dislocation annihilation occurs spontaneously when dipoles approach within a spacing of d_{edge}

$$\dot{\rho}_{\text{ann}}^\alpha = -\frac{2d_{\text{edge}}}{b} \rho^\alpha |\dot{\gamma}^\alpha|. \quad (44)$$

The resolved shear stress τ^α is corrected by replacing with $\tau^{\alpha'}$ and accounting for the latent and self-hardening as

$$\tau^{\alpha'} = \tau^\alpha - \tau_h = \mathbf{P}_{\text{tot}}^\alpha : \sigma - \mu b \sqrt{\sum_{\alpha'} \xi_{\alpha\alpha'} \rho^{\alpha'}}, \quad (45)$$

where τ_h is the hardening stress, $\xi_{\alpha\alpha'}$ are the coefficients of the interaction matrix between slip system α and α' , respectively, as six possible independent interactions: self, coplanar, collinear, orthogonal, glissile, and sessile.

Table 5. Parameters for W used in this case study (cf. Tables 2 and 3 in Cereceda et al. Cereceda et al. (2016, 2015), Section 6.2.4 Roters et al. (2019)). Bounds for τ_{Peierls} are devised based on Samolyuk et al Samolyuk et al. (2012) and Cereceda et al Cereceda et al. (2016).

variable	description	units	reference value	nature	distribution
C_{11}	elastic constant	GPa	523.0	deterministic	–
C_{12}	elastic constant	GPa	202.0	deterministic	–
C_{44}	elastic constant	GPa	161.0	deterministic	–
b	Burgers vector	nm	0.272	deterministic	–
ν_0	initial dislocation glide velocity	m/s	1.0×10^{-4}	stochastic	$\mathcal{U}[10^{-3}, \cdot 10^{-5}]$
ρ_0^α	initial dislocation density	m/m ³	1.0×10^{12}	stochastic	$\mathcal{U}[10^{10}, 5 \cdot 10^{12}]$
τ_{Peierls}	Peierls stress	GPa	2.03	stochastic	$\mathcal{U}[1.64, 2.42]$
p	p -exponent in glide velocity, $0 < p \leq 1$	–	0.32	stochastic	$\mathcal{U}[0.1, 1.0]$
q	q -exponent in glide velocity, $1 \leq q \leq 2$	–	1.46	stochastic	$\mathcal{U}[1.0, 2.0]$
ΔH_0	activation energy for dislocation glide	J	2.725×10^{-19}	stochastic	$\mathcal{U}[1.5, 3.5] \cdot 10^{-19}$
C_λ	dislocation mean free path parameter	–	10	stochastic	$\mathcal{U}[5, 20]$

6.2 Design of numerical experiments

For dislocation-density-based CPFEM simulations, we used an RVE shown in Figure 15a, with the crystallographic texture shown in Figure 15b and Euler angles $(\phi_1, \theta, \phi_2) = (0, 0, 45)$. Average grain size of $3.0339 \mu\text{m}$ is used, where an RVE of size $32 \mu\text{m}^3$ is generated. A mesh of 32^3 is created to approximate the microstructure RVE. In DREAM.3D, the texture crystallography with Euler angles $(\phi_1, \theta, \phi_2) = (0^\circ, 0^\circ, 45^\circ)$ is used, the grain size parameters are set as $\mu_D = 1.0986$, $\sigma_D = 0.15$, which results in a RVE with 2089 grains, shown in Figure 15a. For DAKOTA, we set the sparse grid level $\ell = 3$, dimensionality $n = 17$, which results in 799 inputs. For each set of input parameters, a CPFEM simulation is performed, followed by the post-process. The results are analyzed in the following section. A uniaxial loading condition is applied in the [100] direction with $\dot{\epsilon} = 10^{-3} \text{s}^{-1}$.

To compare with the default parameter, a single CPFEM simulation is performed with constitutive parameters described in Table 5. The stress-strain equivalent curve is shown in Figure 16. As a

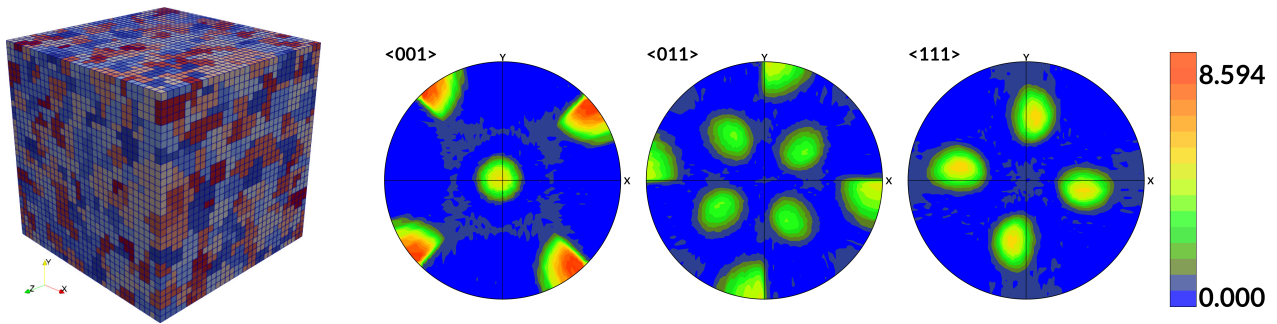


Figure 15a. Representative volume element for W.

Figure 15b. Rotated Cube type of texture component with Euler angles $(\phi_1, \theta, \phi_2) = (0^\circ, 0^\circ, 45^\circ)$.

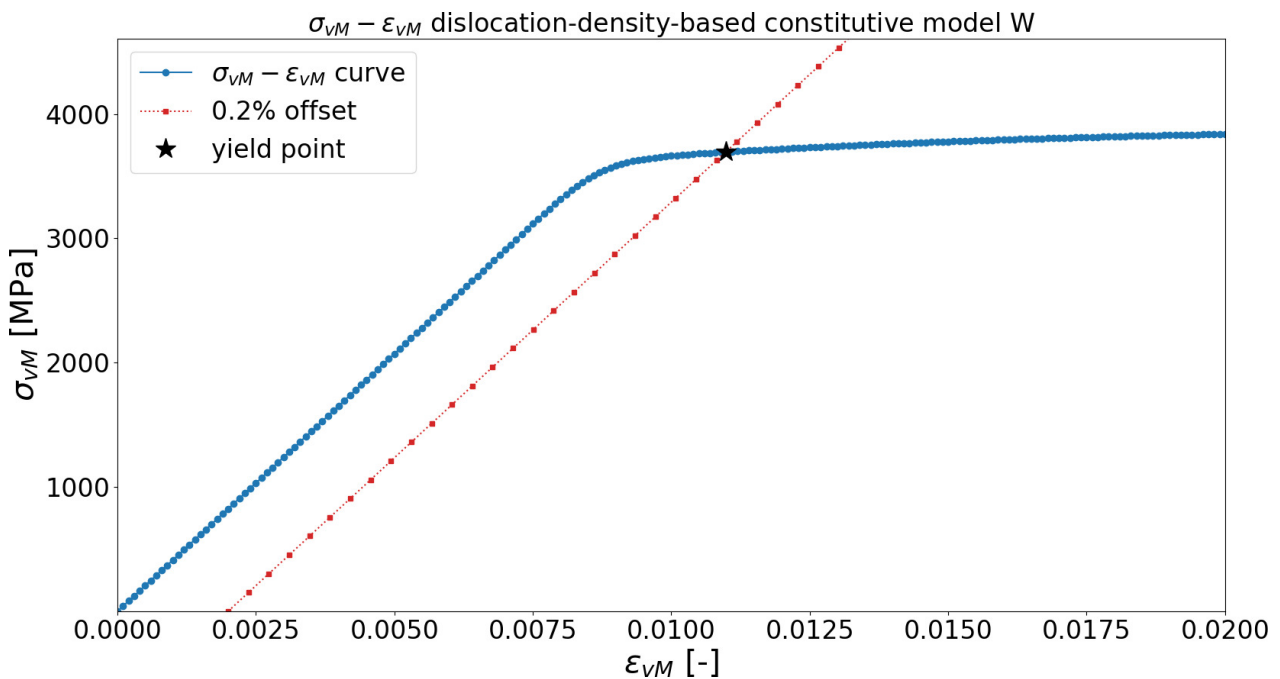


Figure 16. Stress-strain equivalent curve for W with default parameters and determination of yield point. Modulus of elasticity is estimated as 411.3528 GPa, while (ϵ_Y, σ_Y) are estimated as (0.01098, 3695 MPa).

reference to experimental data³, the modulus of elasticity for polycrystalline W is reported at 400 GPa, whereas its yield strength is reported as approximately 750 MPa. Compared to the experiment, the computed modulus agrees very well, but the yield strength σ_Y differs, possibly due to the constitutive model is calibrated for single crystal W, whereas the experimental data is reported for polycrystalline W.

6.3 Numerical results

Figure 17 shows a compilation of stress-strain curves for 799 simulations, where each corresponds to a unique set of constitutive parameters for bcc W. As shown in this figure, the constitutive model

³ <http://www.matweb.com/search/DataSheet.aspx?MatGUID=41e0851d2f3c417ba69ea0188fa570e3>

has a minor effect on the effective modulus of elasticity, and more profound effect on the yield stress σ_Y .

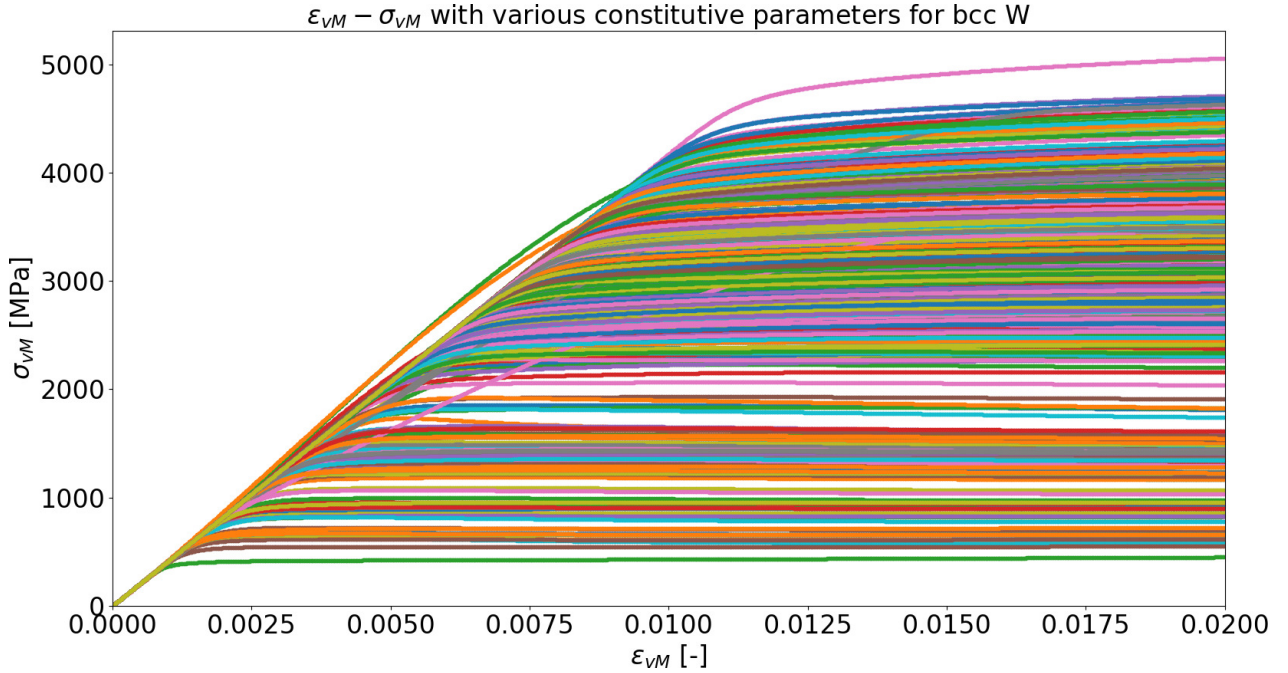


Figure 17. Equivalent $\varepsilon_{vM} - \sigma_{vM}$ plots for bcc W.

Figures 18a and Figure 18b shows the probability density function for ε_Y and σ_Y , respectively. The mode for ε_Y is approximately 0.01010, whereas the mode for σ_Y is approximately 3350 MPa. The uncertainty explained in σ_Y reasonably agree with experimental data. For experimental data with $\sigma_Y \approx 750$ MPa, fairly a few set of parameters can reproduce and calibrate accordingly, as shown in Figure 17.

Figure 19 and Figure 20, respectively, show the Sobol' indices for ε_Y and σ_Y . Ranking from the most influential parameters to the least influential parameters for ε_Y from the Sobol indices for main effects, $T_p = 0.7356$, $T_{\Delta H_0} = 0.212$, $T_{C_\lambda} = 0.2089$, $T_q = 0.1942$, $T_{\rho_0^\alpha} = 0.1556$, $T_{\tau_{\text{Peierls}}} = 0.05712$, $T_{\nu_0} = -0.03444$. Ranking from the most influential parameters to the least influential parameters for σ_Y from the Sobol indices for main effects, $T_p = 0.5668$, $T_{\Delta H_0} = 0.2095$, $T_{C_\lambda} = 0.2079$, $T_q = 0.1795$, $T_{\rho_0^\alpha} = 0.1560$, $T_{\tau_{\text{Peierls}}} = 0.06172$, $T_{\nu_0} = -0.03663$. Since the ranking does not change when the quantity of interest changes from ε_Y to σ_Y , we conclude that the importance of parameters is $p > \Delta H_0 > C_\lambda > q > \rho_0^\alpha > \tau_{\text{Peierls}} > \nu_0$.

7 DISCUSSION

In this paper, we conducted several UQ studies for constitutive models in CPFEM with a single microstructure RVE for each case study. Three case studies are performed with different crystal structures, namely fcc, hcp, and bcc, for Cu, Mg, and W, respectively. In this paper, three materials systems with different crystal structures (fcc, bcc, and hcp) are studied. Depending on the crystal structure, there may be different slipping and twinning systems in terms of slipping and twinning directions in plastic deformation, leading to interesting materials behaviors and mechanisms. The

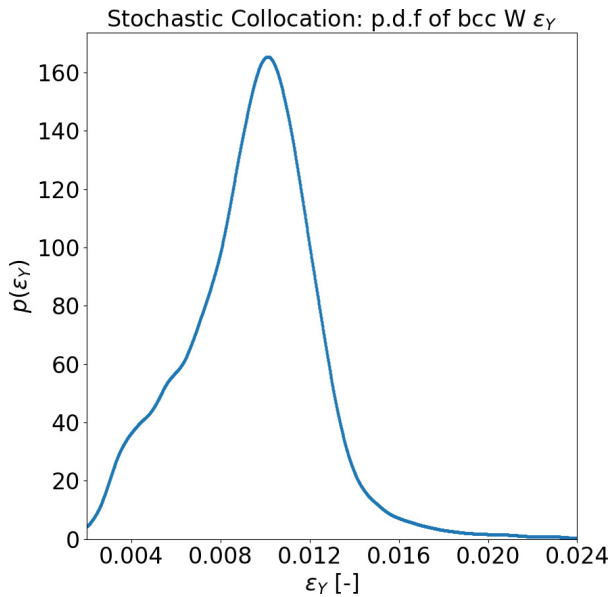


Figure 18a. SC probability density function of ϵ_Y for bcc W.

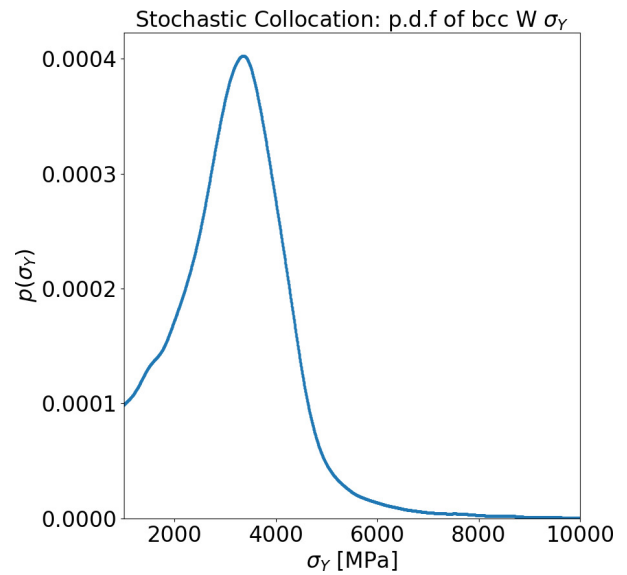


Figure 18b. SC probability density function of σ_Y for bcc W.

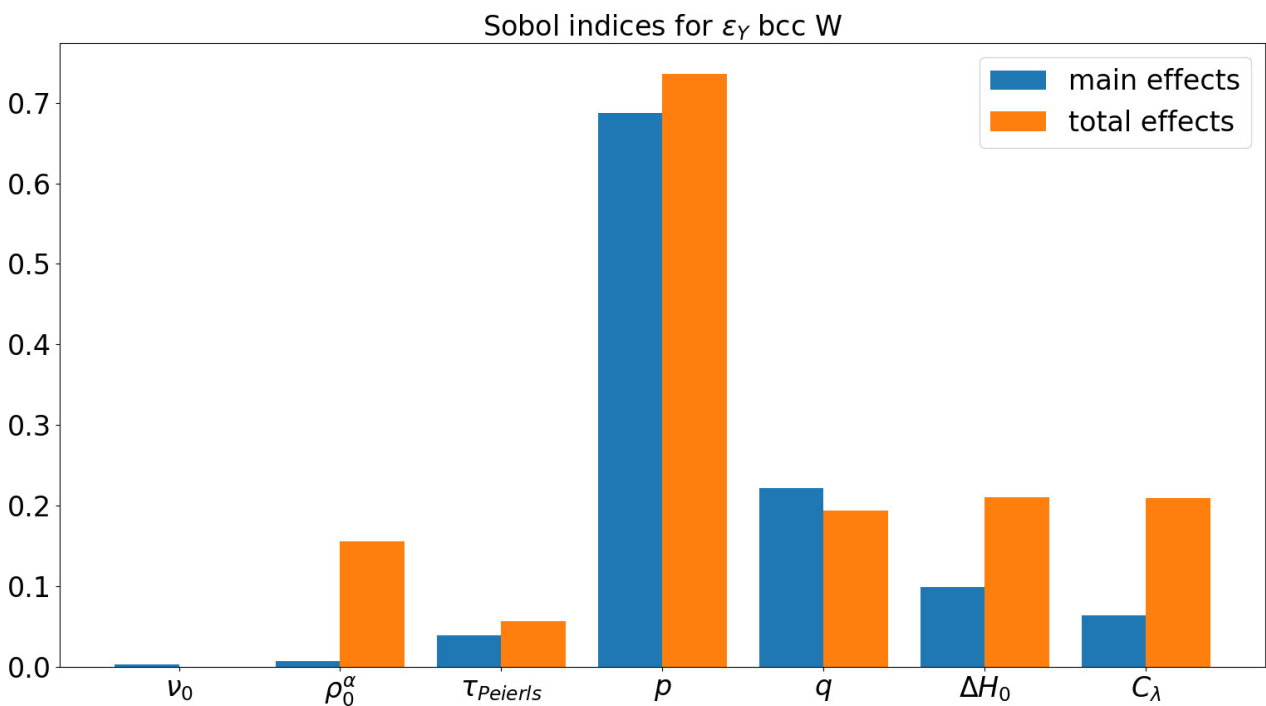


Figure 19. Sobol' indices for ϵ_Y for bcc W.

quantities of interest are selected as the initial yield strain ϵ_Y and the initial yield stress σ_Y . For fcc Cu, parameter τ_0 is the most influential parameter for the initial yield behavior. For hcp Mg, all $\tau_{0,basal}$, $\tau_{0,C2}$, and n_{tw} parameters are influential for the initial yield behavior. For bcc W, p parameter in the short-range activation energy model is the most influential parameter for the initial yield behavior.

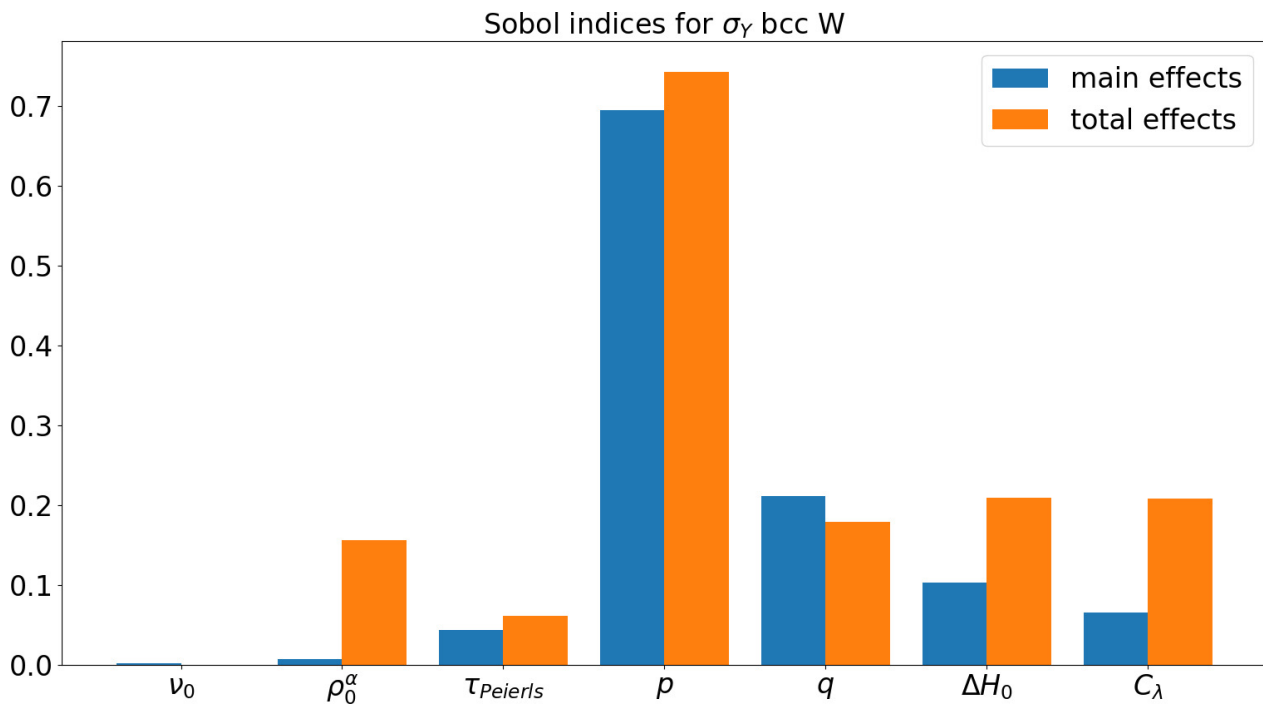


Figure 20. Sobol' indices for σ_Y for bcc W.

UQ studies, such as those described in this manuscript, play an important role in constitutive model calibration for unknown material system in the future. Since there are only a limited number of physical constitutive models, it is important to conduct a UQ study to observe the range of quantities of interest, and to numerically rank the influence of constitutive model parameters. Based on the stress-strain compilation curve conducted for various constitutive model parameters, the material behaviors can be rigorously quantified. The obtained UQ results provide a foundational step for further constitutive model calibration for future works, mostly conducted via digital image correlation techniques Turner et al. (2015); Reu et al. (2018, 2021).

Compared to polynomial approximation with full tensor grid, sparse grid approaches have a significant computational advantages, where this advantage grows with increasing dimensionality thanks to a slower growth rate Nobile et al. (2008). In the context of constitutive models, the computational reduction is mostly profound in the case of hcp system (as opposed to bcc and fcc), such as Mg and Ti, and in the case of dislocation-density-based constitutive model (as opposed to phenomenological model), where many parameters require careful calibration to obtain a sufficient agreement with experiments. For simple system with a relatively simple phenomenological constitutive model, the computational reduction is less severe. It is noteworthy that the level of the Smolyak sparse grid in this study has a little effect on the resulting probability density function of QoIs. This implies that the underlying function is perhaps mostly low-order. This observation can also be confirmed by the Sobol' indices, where the first-order Sobol' indices are much more dominant, compared to higher-order Sobol' indices.

To construct the response surface model, stochastic collocation provides a significant advantage for reducing the curse of dimensionality. However, when it comes to accuracy, Gaussian process regression, which is also the underlying surrogate model for Bayesian optimization, is arguably one

of the best approaches in shallow machine learning. The direction of coupling Bayesian optimization, e.g. Tran et al. (2019a, 2020, 2021); Tran (2019); Tran et al. (2022), for robust constitutive model calibration remains open for future research.

The scope of this manuscript is to quantify the microstructure-sensitive uncertainty. Obviously, it can be expanded to account for the entire stress-strain curve. However, due to the number of parameters involved in each constitutive model, there are hundreds to thousands of runs needed for a single microstructure RVE. Such computationally expensive numerical experiments require careful planning and execution, and therefore, remain a potential topic for future studies. It is important to point out that by restricting to one RVE per case study, this work does not address microstructure-sensitive uncertainty that either is related or induced by the underlying stochastic nature of microstructures. The direction of investigating a microstructure ensemble with many RVEs remain open for future work.

8 CONCLUSION

In this paper, we applied SC to quantify uncertainty associated with the initial yield behavior, mainly the estimated yield strain ε_Y and the estimated yield stress σ_Y for fcc Cu, hcp Mg, and bcc W. A variety of constitutive models are used, resulting with different parameterization and dimensionalities for the constitutive models considered. To mitigate the curse of dimensionality, Smolyak sparse grid is employed for high-dimensional integration to evaluate the PCE coefficients. Variance-based global sensitivity analysis is used to study the sensitivity analysis of the constitutive model parameters.

In light of the computational results presented in previous sections, there are several influential parameters that may have a significant effect on the initial yield behavior. For the phenomenological constitutive model, the slip resistance τ_0 , the slip hardening parameter h_0 , and the strain rate sensitivity parameter n are the most influential parameters, ranking in descending order. For the dislocation-density-based constitutive model, the p -exponent in glide velocity is the most influential parameter, followed by the activation energy for dislocation glide ΔH_0 , the dislocation mean free path parameter C_λ , the q -exponent in glide velocity, and the initial dislocation density ρ_0^α . We conclude that in both constitutive models considered in this study, i.e. phenomenological (with and without twinning) and dislocation-density-based constitutive models, regarding the initial yield behavior, some parameters may have a profound effect on the QoI, while some others may not have a significant effect. The observation could potentially pave way for dimensionality reduction in constitutive model calibration in the future.

CONFLICT OF INTEREST STATEMENT

The authors declare that the research was conducted in the absence of any commercial or financial relationships that could be construed as a potential conflict of interest.

AUTHOR CONTRIBUTIONS

A.T. conceptualizes, performs simulations, analyzes data, and drafts the manuscript. B.T. and T.W. consults in uncertainty quantification aspect. H.L. consults in crystal plasticity finite element aspect.

ACKNOWLEDGMENTS

The views expressed in the article do not necessarily represent the views of the U.S. Department of Energy or the United States Government. Sandia National Laboratories is a multimission laboratory managed and operated by National Technology and Engineering Solutions of Sandia, LLC., a wholly owned subsidiary of Honeywell International, Inc., for the U.S. Department of Energy's National Nuclear Security Administration under contract DE-NA-0003525.

DATA AVAILABILITY STATEMENT

The datasets for this study are available upon reasonable request.

REFERENCES

- Acar, P., Srivastava, S., and Sundararaghavan, V. (2017). Stochastic design optimization of microstructures with utilization of a linear solver. *AIAA Journal* 55, 3161–3168
- [Dataset] Adams, B. M., Bohnhoff, W., Dalbey, K., Eddy, J., Eldred, M., Gay, D., et al. (2009). DAKOTA, a multilevel parallel object-oriented framework for design optimization, parameter estimation, uncertainty quantification, and sensitivity analysis: version 5.0 user's manual. <https://dakota.sandia.gov/>
- Agnew, S., Brown, D., and Tomé, C. (2006). Validating a polycrystal model for the elastoplastic response of magnesium alloy AZ31 using in situ neutron diffraction. *Acta materialia* 54, 4841–4852
- Agrawal, A. and Choudhary, A. (2016). Perspective: Materials informatics and big data: Realization of the “fourth paradigm” of science in materials science. *APL Materials* 4, 053208
- Babuška, I., Nobile, F., and Tempone, R. (2007). A stochastic collocation method for elliptic partial differential equations with random input data. *SIAM Journal on Numerical Analysis* 45, 1005–1034
- Barthelmann, V., Novak, E., and Ritter, K. (2000). High dimensional polynomial interpolation on sparse grids. *Advances in Computational Mathematics* 12, 273–288
- Cerceda, D., Diehl, M., Roters, F., Raabe, D., Perlado, J. M., and Marian, J. (2016). Unraveling the temperature dependence of the yield strength in single-crystal tungsten using atomistically-informed crystal plasticity calculations. *International Journal of Plasticity* 78, 242–265
- Cerceda, D., Diehl, M., Roters, F., Shanthraj, P., Raabe, D., Perlado, J. M., et al. (2015). Linking atomistic, kinetic Monte Carlo and crystal plasticity simulations of single-crystal tungsten strength. *GAMM-Mitteilungen* 38, 213–227
- Cerceda, D., Stukowski, A., Gilbert, M., Queyreau, S., Ventelon, L., Marinica, M.-C., et al. (2013). Assessment of interatomic potentials for atomistic analysis of static and dynamic properties of screw dislocations in W. *Journal of Physics: Condensed Matter* 25, 085702
- Choi, H.-J., McDowell, D. L., Allen, J. K., and Mistree, F. (2008). An inductive design exploration method for hierarchical systems design under uncertainty. *Engineering Optimization* 40, 287–307
- Crestaux, T., Le Maître, O., and Martinez, J.-M. (2009). Polynomial chaos expansion for sensitivity analysis. *Reliability Engineering & System Safety* 94, 1161–1172
- Dalbey, K., Eldred, M., Geraci, G., Jakeman, J., Maupin, K., Monschke, J. A., et al. (2021). *Dakota A Multilevel Parallel Object-Oriented Framework for Design Optimization Parameter Estimation*

- Uncertainty Quantification and Sensitivity Analysis: Version 6.14 Theory Manual*. Tech. rep., Sandia National Lab.(SNL-NM), Albuquerque, NM (United States)
- Diehl, M., Groeber, M., Haase, C., Molodov, D. A., Roters, F., and Raabe, D. (2017). Identifying structure–property relationships through DREAM.3D representative volume elements and DAMASK crystal plasticity simulations: An integrated computational materials engineering approach. *JOM* 69, 848–855
- Eldred, M. (2009). Recent advances in non-intrusive polynomial chaos and stochastic collocation methods for uncertainty analysis and design. In *50th AIAA/ASME/ASCE/AHS/ASC Structures, Structural Dynamics, and Materials Conference 17th AIAA/ASME/AHS Adaptive Structures Conference 11th AIAA No. 2274*
- Eldred, M. and Burkardt, J. (2009). Comparison of non-intrusive polynomial chaos and stochastic collocation methods for uncertainty quantification. In *47th AIAA aerospace sciences meeting including the new horizons forum and aerospace exposition*. 976
- Ellis, B. D. and McDowell, D. L. (2017). Application-specific computational materials design via multiscale modeling and the inductive design exploration method (IDEM). *Integrating materials and manufacturing innovation* 6, 9–35
- Fernandez-Zelaia, P., Joseph, V. R., Kalidindi, S. R., and Melkote, S. N. (2018). Estimating mechanical properties from spherical indentation using Bayesian approaches. *Materials & Design* 147, 92–105
- Fritsch, F. N. and Butland, J. (1984). A method for constructing local monotone piecewise cubic interpolants. *SIAM journal on scientific and statistical computing* 5, 300–304
- Groeber, M. A. and Jackson, M. A. (2014). DREAM. 3D: a digital representation environment for the analysis of microstructure in 3D. *Integrating materials and manufacturing innovation* 3, 5
- Honarmandi, P. and Arróyave, R. (2020). Uncertainty quantification and propagation in computational materials science and simulation-assisted materials design. *Integrating Materials and Manufacturing Innovation* , 1–41
- Hutchinson, J. W. (1976). Bounds and self-consistent estimates for creep of polycrystalline materials. *Proceedings of the Royal Society of London. A. Mathematical and Physical Sciences* 348, 101–127
- Kalidindi, S. R. (1998). Incorporation of deformation twinning in crystal plasticity models. *Journal of the Mechanics and Physics of Solids* 46, 267–290
- Kalidindi, S. R., Medford, A. J., and McDowell, D. L. (2016). Vision for data and informatics in the future materials innovation ecosystem. *JOM* 68, 2126–2137
- Kocks, U. F., Tomé, C. N., and Wenk, H.-R. (1998). *Texture and anisotropy: preferred orientations in polycrystals and their effect on materials properties* (Cambridge university press)
- Koester, A., Ma, A., and Hartmaier, A. (2012). Atomistically informed crystal plasticity model for body-centered cubic iron. *Acta Materialia* 60, 3894–3901
- Kotha, S., Ozturk, D., and Ghosh, S. (2019a). Parametrically homogenized constitutive models (PHCMs) from micromechanical crystal plasticity FE simulations, part I: Sensitivity analysis and parameter identification for Titanium alloys. *International Journal of Plasticity* 120, 296–319
- Kotha, S., Ozturk, D., and Ghosh, S. (2019b). Parametrically homogenized constitutive models (PHCMs) from micromechanical crystal plasticity FE simulations: Part II: Thermo-elasto-plastic model with experimental validation for titanium alloys. *International Journal of Plasticity* 120, 320–339

- Kotha, S., Ozturk, D., and Ghosh, S. (2020a). Uncertainty-quantified parametrically homogenized constitutive models (uq-phcms) for dual-phase α/β titanium alloys. *npj Computational Materials* 6, 1–20
- Kotha, S., Ozturk, D., Smarslok, B., and Ghosh, S. (2020b). Uncertainty quantified parametrically homogenized constitutive models for microstructure-integrated structural simulations. *Integrating Materials and Manufacturing Innovation* 9, 322–338
- Lim, H., Battaile, C. C., Bishop, J. E., and Foulk III, J. W. (2019). Investigating mesh sensitivity and polycrystalline RVEs in crystal plasticity finite element simulations. *International Journal of Plasticity* 121, 101–115
- Mangal, A. and Holm, E. A. (2018). A dataset of synthetic hexagonal close packed 3d polycrystalline microstructures, grain-wise microstructural descriptors and grain averaged stress fields under uniaxial tensile deformation for two sets of constitutive parameters. *Data in brief* 21, 1833–1841
- McDowell, D. L. (2007). Simulation-assisted materials design for the concurrent design of materials and products. *JOM* 59, 21–25
- McDowell, D. L., Panchal, J., Choi, H.-J., Seepersad, C., Allen, J., and Mistree, F. (2009). *Integrated design of multiscale, multifunctional materials and products* (Butterworth-Heinemann)
- Mecking, H. and Kocks, U. (1981). Kinetics of flow and strain-hardening. *Acta metallurgica* 29, 1865–1875
- Najm, H. N. (2009). Uncertainty quantification and polynomial chaos techniques in computational fluid dynamics. *Annual Review of Fluid Mechanics* 41, 35–52
- Nobile, F., Tamellini, L., and Tempone, R. (2016). Convergence of quasi-optimal sparse-grid approximation of Hilbert-space-valued functions: application to random elliptic PDEs. *Numerische Mathematik* 134, 343–388
- Nobile, F., Tempone, R., and Webster, C. G. (2008). A sparse grid stochastic collocation method for partial differential equations with random input data. *SIAM Journal on Numerical Analysis* 46, 2309–2345
- Novak, E. and Ritter, K. (1996). High dimensional integration of smooth functions over cubes. *Numerische Mathematik* 75, 79–97
- Novak, E. and Ritter, K. (1997). The curse of dimension and a universal method for numerical integration. In *Multivariate approximation and splines* (Springer). 177–187
- Novak, E. and Ritter, K. (1999). Simple cubature formulas with high polynomial exactness. *Constructive approximation* 15, 499–522
- Ozturk, D., Kotha, S., Pilchak, A. L., and Ghosh, S. (2019a). Parametrically homogenized constitutive models (PHCMs) for multi-scale predictions of fatigue crack nucleation in titanium alloys. *JOM* 71, 2657–2670
- Ozturk, D., Kotha, S., Pilchak, A. L., and Ghosh, S. (2019b). Two-way multi-scaling for predicting fatigue crack nucleation in titanium alloys using parametrically homogenized constitutive models. *Journal of the Mechanics and Physics of Solids* 128, 181–207
- Panchal, J. H., Kalidindi, S. R., and McDowell, D. L. (2013). Key computational modeling issues in integrated computational materials engineering. *Computer-Aided Design* 45, 4–25
- Pham, M.-S., Creuziger, A., Iadicola, M., and Rollett, A. D. (2017). Roles of texture and latent hardening on plastic anisotropy of face-centered-cubic materials during multi-axial loading. *Journal of the Mechanics and Physics of Solids* 99, 50–69

- Raabe, D. and Roters, F. (2004). Using texture components in crystal plasticity finite element simulations. *International Journal of Plasticity* 20, 339–361
- Raabe, D., Zhao, Z., Park, S.-J., and Roters, F. (2002). Theory of orientation gradients in plastically strained crystals. *Acta Materialia* 50, 421–440
- Reu, P., Blaysat, B., Andò, E., Bhattacharya, K., Couture, C., Couty, V., et al. (2021). DIC challenge 2.0: Developing images and guidelines for evaluating accuracy and resolution of 2D analyses focus on the metrological efficiency indicator. *Experimental Mechanics*
- Reu, P. L., Toussaint, E., Jones, E., Bruck, H. A., Iadicola, M., Balcaen, R., et al. (2018). DIC challenge: developing images and guidelines for evaluating accuracy and resolution of 2d analyses. *Experimental Mechanics* 58, 1067–1099
- Roters, F., Diehl, M., Shanthraj, P., Eisenlohr, P., Reuber, C., Wong, S. L., et al. (2019). DAMASK—The Düsseldorf Advanced Material Simulation Kit for modeling multi-physics crystal plasticity, thermal, and damage phenomena from the single crystal up to the component scale. *Computational Materials Science* 158, 420–478
- Saltelli, A., Annoni, P., Azzini, I., Campolongo, F., Ratto, M., and Tarantola, S. (2010). Variance based sensitivity analysis of model output. design and estimator for the total sensitivity index. *Computer physics communications* 181, 259–270
- Samolyuk, G. D., Osetsky, Y., and Stoller, R. (2012). The influence of transition metal solutes on the dislocation core structure and values of the peierls stress and barrier in tungsten. *Journal of Physics: Condensed Matter* 25, 025403
- Sedighiani, K., Diehl, M., Traka, K., Roters, F., Sietsma, J., and Raabe, D. (2020). An efficient and robust approach to determine material parameters of crystal plasticity constitutive laws from macro-scale stress–strain curves. *International Journal of Plasticity* 134, 102779
- Sedighiani, K., Traka, K., Roters, F., Raabe, D., Sietsma, J., and Diehl, M. (2022). Determination and analysis of the constitutive parameters of temperature-dependent dislocation-density-based crystal plasticity models. *Mechanics of Materials* 164, 104117
- Smolyak, S. A. (1963). Quadrature and interpolation formulas for tensor products of certain classes of functions. In *Doklady Akademii Nauk* (Russian Academy of Sciences), vol. 148, 1042–1045
- Stukowski, A., Cereceda, D., Swinburne, T. D., and Marian, J. (2015). Thermally-activated non-Schmid glide of screw dislocations in W using atomistically-informed kinetic Monte Carlo simulations. *International Journal of Plasticity* 65, 108–130
- Sudret, B. (2008). Global sensitivity analysis using polynomial chaos expansions. *Reliability engineering & system safety* 93, 964–979
- Tallman, A. E., Stopka, K. S., Swiler, L. P., Wang, Y., Kalidindi, S. R., and McDowell, D. L. (2019). Gaussian-process-driven adaptive sampling for reduced-order modeling of texture effects in polycrystalline alpha-Ti. *JOM* 71, 2646–2656
- Tallman, A. E., Swiler, L. P., Wang, Y., and McDowell, D. L. (2020). Uncertainty propagation in reduced order models based on crystal plasticity. *Computer Methods in Applied Mechanics and Engineering* 365, 113009
- Tang, G., Iaccarino, G., and Eldred, M. (2010). Global sensitivity analysis for stochastic collocation. In *51st AIAA/ASME/ASCE/AHS/ASC Structures, Structural Dynamics, and Materials Conference 18th AIAA/ASME/AHS Adaptive Structures Conference 12th*. 2922
- Tran, A. (2019). aphBO-2GP-3B: A budged asynchronously-parallel multi-acquisition for known/unknown constrained Bayesian optimization on HPC. *GIW Internal Reports*

- Tran, A., Eldred, M., Wildey, T., McCann, S., Sun, J., and Visintainer, R. J. (2022). aphBO-2GP-3B: a budgeted asynchronous parallel multi-acquisition functions for constrained Bayesian optimization on high-performing computing architecture. *Structural and Multidisciplinary Optimization* 65, 1–45
- Tran, A., Eldred, M. S., McCann, S., and Wang, Y. (2021). srMO-BO-3GP: A sequential regularized multi-objective Bayesian optimization for constrained design applications using an uncertain Pareto classifier. *Journal of Mechanical Design* , 1–15
- Tran, A., Sun, J., Furlan, J. M., Pagalthivarthi, K. V., Visintainer, R. J., and Wang, Y. (2019a). pBO-2GP-3B: A batch parallel known/unknown constrained Bayesian optimization with feasibility classification and its applications in computational fluid dynamics. *Computer Methods in Applied Mechanics and Engineering* 347, 827–852
- Tran, A. and Wildey, T. (2020). Solving stochastic inverse problems for property-structure linkages using data-consistent inversion and machine learning. *JOM* 73, 72–89
- Tran, A., Wildey, T., and McCann, S. (2020). sMF-BO-2CoGP: A sequential multi-fidelity constrained Bayesian optimization for design applications. *Journal of Computing and Information Science in Engineering* 20, 1–15
- Tran, A. V., Liu, D., Tran, H. A., and Wang, Y. (2019b). Quantifying uncertainty in the process-structure relationship for Al-Cu solidification. *Modelling and Simulation in Materials Science and Engineering* 27, 064005
- Tromans, D. (2011). Elastic anisotropy of HCP metal crystals and polycrystals. *Int. J. Res. Rev. Appl. Sci* 6, 462–483
- Turner, D., Crozier, P., and Reu, P. (2015). *Digital image correlation engine*. Tech. rep., Sandia National Laboratories (SNL), Albuquerque, NM, and Livermore, CA . . .
- Wang, F., Sandlöbes, S., Diehl, M., Sharma, L., Roters, F., and Raabe, D. (2014). In situ observation of collective grain-scale mechanics in Mg and Mg–rare earth alloys. *Acta materialia* 80, 77–93
- Wasilkowski, G. W. and Woźniakowski, H. (1995). Explicit cost bounds of algorithms for multivariate tensor product problems. *Journal of Complexity* 11, 1–56
- Weber, G., Pinz, M., and Ghosh, S. (2020). Machine learning-aided parametrically homogenized crystal plasticity model (PHCPM) for single crystal Ni-based superalloys. *JOM* 72, 4404–4419
- Weirs, V. G., Kamm, J. R., Swiler, L. P., Tarantola, S., Ratto, M., Adams, B. M., et al. (2012). Sensitivity analysis techniques applied to a system of hyperbolic conservation laws. *Reliability Engineering & System Safety* 107, 157–170
- Wenk, H.-R. and Van Houtte, P. (2004). Texture and anisotropy. *Reports on Progress in Physics* 67, 1367
- Xiu, D. (2009). Fast numerical methods for stochastic computations: a review. *Communications in computational physics* 5, 242–272
- Xiu, D. and Karniadakis, G. E. (2002). The Wiener–Askey polynomial chaos for stochastic differential equations. *SIAM Journal on Scientific Computing* 24, 619–644
- Zhao, Z., Ruiz, M. R., Lu, J., Monclús, M. A., Molina-Aldareguía, J. M., Bieler, T. R., et al. (2022). Quantifying the uncertainty of critical resolved shear stress values derived from nano-indentation in hexagonal Ti alloys. *Experimental Mechanics* , 1–13